



저작자표시-비영리-변경금지 2.0 대한민국

이용자는 아래의 조건을 따르는 경우에 한하여 자유롭게

- 이 저작물을 복제, 배포, 전송, 전시, 공연 및 방송할 수 있습니다.

다음과 같은 조건을 따라야 합니다:



저작자표시. 귀하는 원저작자를 표시하여야 합니다.



비영리. 귀하는 이 저작물을 영리 목적으로 이용할 수 없습니다.



변경금지. 귀하는 이 저작물을 개작, 변형 또는 가공할 수 없습니다.

- 귀하는, 이 저작물의 재이용이나 배포의 경우, 이 저작물에 적용된 이용허락조건을 명확하게 나타내어야 합니다.
- 저작권자로부터 별도의 허가를 받으면 이러한 조건들은 적용되지 않습니다.

저작권법에 따른 이용자의 권리는 위의 내용에 의하여 영향을 받지 않습니다.

이것은 [이용허락규약\(Legal Code\)](#)을 이해하기 쉽게 요약한 것입니다.

[Disclaimer](#)

공학박사 학위논문

**Cathode | Electrolyte Interface  
Engineering using Organic Molecules  
for Li-O<sub>2</sub> and Li-ion Batteries**

유기 분자를 이용한 리튬-산소 전지와 리튬-이온  
전지의 양극 | 전해질 계면 개질 연구

2020년 2월

서울대학교 대학원

화학생물공학부

정 성 은

**Cathode | Electrolyte Interface Engineering**  
**using Organic Molecules**  
**for Li-O<sub>2</sub> and Li-ion Batteries**

지도 교수 최 장 욱

이 논문을 공학박사 학위논문으로 제출함  
2020년 2월

서울대학교 대학원  
화학생물공학부  
정 성 은

정성은의 공학박사 학위논문을 인준함  
2020년 2월

위 원 장 \_\_\_\_\_ 성 영 은 \_\_\_\_\_ (인)

부위원장 \_\_\_\_\_ 최 장 욱 \_\_\_\_\_ (인)

위 원 \_\_\_\_\_ 이 규 태 \_\_\_\_\_ (인)

위 원 \_\_\_\_\_ 조 용 남 \_\_\_\_\_ (인)

위 원 \_\_\_\_\_ 김 기 재 \_\_\_\_\_ (인)

# Abstract

## **Cathode | Electrolyte Interface Engineering using Organic Molecules for Li–O<sub>2</sub> and Li–ion Batteries**

Sung Eun Jerng

Department of Chemical and Biological Engineering

The Graduate School

Seoul National University

The rapidly increasing usage of portable electronic devices and electric vehicles have consistently demanded high energy density batteries. While commercial lithium-ion batteries (LIBs) are consisted of layered oxide cathode materials, LiCoO<sub>2</sub>, the low specific capacity (145 mAh g<sup>-1</sup>) and scarcity of cobalt reserves have arisen the investigations on alternative cathode materials such as oxygen and high-Ni LiNi<sub>x</sub>Co<sub>y</sub>Mn<sub>z</sub>O<sub>2</sub> (NCM).

The lithium-oxygen (Li–O<sub>2</sub>) batteries have been a promising high energy density battery system attributed to the high theoretical specific energy of 3458 Wh kg<sup>-1</sup>. However, their low cycle life originated from the large overpotential has inhibited them from practical use. Especially, the sluggish charging process has derived the charging overpotential larger than that of discharge. Thus, various catalysts were applied to the cathode electrode to reduce facilitate charging of lithium-oxygen battery. In chapter 2, the ligand modified heme catalysts were applied to the cathode of Li–O<sub>2</sub> battery to reduce the charging overpotential and

enhance the cycle life. According to the applied ligands of heme structure, the lewis acidity at the Fe active sites varied and affected the electrochemical performance of the cells. Furthermore, the origin of the different catalytic activity among various ligands were revealed using density functional theory (DFT) along with each charging steps.

In addition, high-Ni NCM have attracted attentions owing to its high specific capacity of  $>200 \text{ mAh g}^{-1}$  and comparably reasonable price of nickel. However, as the content of nickel becomes higher, the structural stability of the layered oxide decreases due to large volume change of the layer structure, transition metal (TM) mixing and TM dissolution. Thus, the surface engineering to protect the surface of the high-Ni NCM without disturbing the electronic/ionic conductivity is crucial in preventing the degradation of high-Ni NCM. In chapter 3, the pyrazine linked covalent organic frameworks (Pyr-2D) were coated on the high-Ni NCM. The Pyr-2D provides electronic/ionic conductive layer on the high-Ni NCM through its unique rigid and porous structure. Moreover, the preformed transition metal mixed layer combined with Pyr-2D showed improved cycle life and rate capability due to prevention of TM mixing and dissolution of transition metal during cycling.

This thesis on the cathode catalysts design (chapter 2) and surface modification of cathode materials (chapter 3) would provide logical designing strategies toward electrolyte/cathode interface engineering to enhance the charge/discharge cycle life of lithium batteries.

**Keywords:** cathode catalyst, heme, covalent-organic framework, high-Ni NCM, Li-O<sub>2</sub> battery, Li-ion battery

**Student Number:** 2016-39189

# Table of Contents

<b>Abstract .....</b>	<b>i</b>
<b>Table of Contents.....</b>	<b>iii</b>
<b>List of Figures .....</b>	<b>v</b>
<b>List of Tables .....</b>	<b>ix</b>
<b>Chapter 1. Introduction .....</b>	<b>1</b>
1.1 Lithium-Oxygen Battery .....	1
1.2 High-Nickel Li[Ni,Co,Mn]O <sub>2</sub> Battery .....	3
1.3 Cathode   Electrolyte Interface Engineering in Battery .....	5
<b>Chapter 2. Lewis Acidity Controlled Heme Catalyst for Lithium-Oxygen Battery .....</b>	<b>6</b>
2.1 Introduction .....	6
2.2 Experimental .....	8
2.2.1 Synthesis of Heme, Heme+NCS and Heme+N <sub>3</sub> Catalysts.....	8
2.2.2 Nitroblue Tetrazolium (NBT) Reduction Test.....	8
2.2.3 Characterization of Heme, Heme+NCS and Heme+N <sub>3</sub> .....	9
2.2.4 Li-O <sub>2</sub> Battery Preparation and Electrochemical Measurements.....	10
2.2.5 Computational Details .....	10
2.3 Results and Discussion .....	12
2.3.1 Characterization of Heme Catalysts.....	12

2.3.2	Electrochemical Performance .....	16
2.3.3	Density Functional Theory (DFT) Calculations.....	30
2.4	Conclusion .....	40

## **Chapter 3. Pyrazine-linked 2D Covalent Organic**

### **Frameworks as Coating Material for High-Nickel**

### **Layered Oxide Cathodes in Lithium-Ion Batteries .41**

3.1	Introduction.....	41
3.2	Experimental .....	44
3.2.1	Synthesis of the Materials.....	44
3.2.2	Characterization of Materials.....	44
3.2.3	Electrochemical Evaluation .....	46
3.3	Results and Discussion .....	47
3.3.1	Characterization of NCM811-Pyr-2D.....	47
3.3.2	Electrochemical Performance .....	59
3.3.3	Effect of Pyr-2D Coating .....	68
3.4	Conclusion .....	72

## **Chapter 4. Summary.....73**

## **Bibliography.....74**

## **Abstract in Korean.....91**

## List of Figures

Figure 2.1	Atomic configurations of (a) Heme, (b) Heme+NCS, and (c) Heme+N <sub>3</sub> . (d) FTIR spectra of the three samples. (e) UV-vis spectra showing NBT reduction by superoxide radical scavenge..13
Figure 2.2	FTIR profiles of Heme+NCS and Heme+N <sub>3</sub> before and after a washing process during synthesis..... 14
Figure 2.3	(a) UV-vis absorbance of NBT at relative radical concentrations of 0.25 C, 0.5 C, 0.75 C and 1 C. 1 C is the concentration of the initial radical solution. (b) Correlation of NBT absorbance at 560 nm with the relative radical concentration..... 15
Figure 2.4	(a) 1st discharge/charge profiles and (b) cyclic voltammetry curves in the potential range of 2.3 to 4.5 V at a scan rate of 0.1 mV s <sup>-1</sup> . Enlarged cyclic voltammetry profiles in the potential range of (c) 3.3~4.3 V and (d) 4.0~4.5 V for Heme, Heme+NCS, and Heme+N <sub>3</sub> electrodes..... 19
Figure 2.5	Cyclic voltammetry profiles of (a) Heme, (b) Heme+NCS and (c) Heme+N <sub>3</sub> when scanned at 0.1 mV s <sup>-1</sup> for 5 cycles... ..20
Figure 2.6	Cycling performance with a fixed capacity of 500 mAh g <sup>-1</sup> at a current density of (a) 100 mA g <sup>-1</sup> and (b) 250 mA g <sup>-1</sup> , with the right y-axes indicating terminal charge voltage.....21
Figure 2.7	(a,b) SEM and (c) FTIR results of Heme and Heme+N <sub>3</sub> air-cathodes after 50 cycles in Figure 2.6 .....22
Figure 2.8	Discharge-charge profiles of (a,b) Heme, (c,d) Heme+NCS, (e,f) Heme+N <sub>3</sub> at 100 and 250 mAh g <sup>-1</sup> ..... 23
Figure 2.9	SEM images of (a,b) Heme, (c,d) Heme+NCS and (e,f) Heme+N <sub>3</sub> air-cathodes after 1 <sup>st</sup> discharge and 1 <sup>st</sup> charge, respectively.....24
Figure 2.10	(a) Cycling performance of Heme, Heme+NCS, and Heme+N <sub>3</sub> at 250 mA g <sup>-1</sup> with a fixed capacity of 1000 mAh g <sup>-1</sup> and (b-d) their

	respective discharge-charge profiles at different cycle numbers.....	25
Figure 2.11	XPS profiles of Heme, Heme+NCS and Heme+N <sub>3</sub> electrodes after (a) 1 <sup>st</sup> discharge, (b) 10 <sup>th</sup> discharge, and (c) 1 <sup>st</sup> full discharge.....	26
Figure 2.12	XRD profiles of Heme, Heme+NCS and Heme+N <sub>3</sub> electrodes after (a) 1 <sup>st</sup> discharge, (b) 10 <sup>th</sup> discharge, and (c) 1 <sup>st</sup> full discharge.....	27
Figure 2.13	SEM images of (a,b,c) Heme, (d,e,f) Heme+NCS, and (g,h,i) Heme+N <sub>3</sub> air-cathodes after 1 <sup>st</sup> discharge, 10 <sup>th</sup> discharge, and 1 <sup>st</sup> full discharge, respectively.....	28
Figure 2.14	The top-view and cross-section SEM images and EDX analysis of Li metal anodes after 10 cycles for (a,b,g) Heme, (c,d,h) Heme+NCS and (e,f,i) Heme+N <sub>3</sub> cathodes.....	29
Figure 2.15	Electrostatic potential map and Mulliken charge distributions of (a) Heme, (b) Heme+NCS, and (c) Heme+N <sub>3</sub> . (d) XPS spectra of the three samples at the N 1s branch.....	33
Figure 2.16	XPS spectra of (a) Heme, (b) Heme+NCS and (c) Heme+N <sub>3</sub> in N 1s branch.....	34
Figure 2.17	XPS spectra of (a) Heme, (b) Heme+NCS and (c) Heme+N <sub>3</sub> in Fe 2p branch.....	35
Figure 2.18	(a) Energy profiles of Heme, Heme+NCS, and Heme+N <sub>3</sub> along the course of charging process. (b) Molecular structures of Heme, Heme+NCS and Heme+N <sub>3</sub> at each charging step. (c) Electron configuration of Fe–O <sub>2</sub> bond upon O <sub>2</sub> adsorption.....	36
Figure 2.19	Molecular structures of Heme, Heme+NCS and Heme+N <sub>3</sub> at the charging step 2. The mulliken charge of the Li <sup>+</sup> in LiO <sub>2</sub> <sup>*</sup> and the nitrogen in the porphyrin ring is denoted.....	37
Figure 2.20	Full discharge profiles of Heme, Heme+NCS and Heme+N <sub>3</sub> electrodes.....	38
Figure 2.21	Overpotentials and desorption energies of Heme, Heme+NCS and	

	Heme+N <sub>3</sub> in correlation with the Mulliken charge of Fe.....	39
Figure 3.1	Synthesis scheme of pyrazine-linked 2D sheet (Pyr-2D) and graphical illustration of NCM811 coated with the Pyr-2D sheet (NCM811-Pyr-2D).....	50
Figure 3.2	Cs-TEM images of (a) bare NCM811 and (b) NCM811 -Pyr-2D. (c) TEM-EDX elemental mapping of NCM811-Pyr-2D with respect to Ni, Co, Mn, C, and N. (d) FT-IR spectra of Pyr-2D and NCM811-Pyr-2D. (e) XRD patterns of bare NCM811 and NCM811-Pyr-2D. Cs-STEM images of (f) bare NCM811 and (g) NCM811-Pyr-2D in the pristine state.....	51
Figure 3.3	Thermogravimetric analysis (TGA) profiles of bare NCM, NCM-Pyr-2Dx1, NCM-Pyr-2Dx5, benzenetetramine, hexaketocyclohexane and Pyr-2D.....	52
Figure 3.4	XRD patterns of bare NCM and NCM811-preformed-TM.....	53
Figure 3.5	XPS of as-prepared (a) bare NCM811 and (b) NCM811-Pyr-2D in the pristine state.....	54
Figure 3.6	Electronic conductivity of bare NCM, NCM-Pyr-2Dx1, NCM-Pyr-2Dx5, and Pyr-2D before and after annealing.....	55
Figure 3.7	Cyclic-voltammetry of (a) bare NCM811 and (b) NCM811-Pyr-2D. Profiles of peak intensity versus square root of scan rate for (c) bare NCM811 and (d) NCM811-Pyr-2D.....	57
Figure 3.8	Cyclic voltammetry profile of Pyr-2D at 1C rate.....	62
Figure 3.9	(a) 1 <sup>st</sup> charge-discharge profiles at the 0.1C rate. (b) cycling and (c) rate performance of bare NCM811 and NCM811-Pyr-2D.....	63
Figure 3.10	Charge-discharge profiles of (a) bare NCM811 and (b) NCM811-Pyr-2D at different cycle numbers when measured at 1C rate.....	64
Figure 3.11	Electrochemical impedance spectroscopy profiles of (a) bare NCM811 and (b) NCM811-Pyr-2D after the 50 <sup>th</sup> and 100 <sup>th</sup> charge	

	cycles. XPS spectra in the F 1s branch after 100 cycles: (c) bare NCM811 and (d) NCM811-Pyr-2D.....	65
Figure 3.12	Electrochemical impedance spectroscopy profiles of NCM811-preformed-TM after the 50 <sup>th</sup> and 100 <sup>th</sup> charge cycle.....	66
Figure 3.13	(a) XRD pattern of bare NCM811 and NCM811-Pyr-2D after 100 <sup>th</sup> charge. Cs-STEM bright field images of (b) bare NCM811 and (c) NCM811-Pyr-2D after 100 <sup>th</sup> charge.....	67
Figure 3.14	Effect of varied amounts of dissolved (a) Ni, (b) Co, and (c) Mn ions from 1 <sup>st</sup> charged NCM811 and NCM811-Pyr-2D at 60 °C. (d) DSC profiles of bare NCM811 and NCM811-Pyr-2D with 1 M LiPF <sub>6</sub> EC:DEC(1:1) electrolyte after 1 <sup>st</sup> delithiation. (e) Cycling performance of the bare NCM811 and NCM811-Pyr-2D at 60 °C when measured at 1C.....	70
Figure 3.15	(a) Cycling performance of bare NCM811, NCM811-preformed-TM, benzenetetramine coated NCM911, hexaketocyclohexane coated NCM811 and NCM811-Pyr-2D. (b) Cycling performance of NCM-Pyr-2D with regard to discharging capacity after different days of air exposure.....	71

## List of Tables

Table 3.1	Electronic conductivity of representative conductive materials in comparison with those in the current work. ....	56
Table 3.2	Lithium ion diffusion coefficients in (a) bare NCM811 and (b) NCM811-Pyr-2D electrodes derived from Figure 3.7 .....	58

# Chapter 1. Introduction

## 1.1 Lithium-Oxygen Battery

High energy density energy storage devices have been a global demand since the emerging electric vehicles and portable electronics.<sup>1</sup> Among the various energy storage systems, lithium oxygen battery has been a promising candidate due to its high theoretical energy density<sup>2</sup> of  $3,600 \text{ Wh kg}^{-1}$  which arise from its unique charge/discharge mechanism; Unlike conventional lithium ion batteries (LIBs) in which lithium ions are intercalated in layered oxide cathode materials during discharge, the lithium ions react with oxygen molecules to produce lithium peroxide in the lithium-oxygen battery.<sup>3</sup>

However, the short cycle life of the present lithium-oxygen battery hinders its practical use.<sup>4</sup> Particularly, the lithium peroxide discharge product which is an electrical insulator, promotes the large charging overpotential accelerating the electrolyte/carbon electrode decompositions.<sup>5</sup> Hitherto, various inorganic/organic catalysts were developed to facilitate the dissociation of the discharge products and to enhance the cycle life.

Since the cathode reaction of Li-O<sub>2</sub> battery is composed of oxygen reduction reaction (ORR) and oxygen evolution reaction (OER), noble metal and metal oxides electrocatalysts were widely applied to the air cathode. Lu et al. synthesized bifunctional Pt/Au catalysts to reduce charge and discharge overpotentials.<sup>6</sup> However, due to the expensive cost and the carbon dissociation from the active noble catalysts, the metal oxide catalysts were investigated to develop environmentally friendly and cheaper catalysts. Jung et al. fabricated vertically aligned carbon nanotube-ruthenium oxide core-shell cathode (VACNT@RuO<sub>2</sub>) and delivered excellent rate capability and cycling stability.<sup>7</sup> The ruthenium shell prevented direct contact between carbon cathode and reactive

oxygen species resulting in cycle stability of Li-O<sub>2</sub> battery. Gong et al. reported that the NiCo<sub>2</sub>O<sub>4</sub> nanoparticles on the N-doped graphene as an efficient bifunctional catalysts.<sup>8</sup> The three-dimensional rGO provided high surface and porosity together with electronic conductivity. As a result, the NCM@N-rGO delivered specific discharge capacity of 6716 mA h g<sup>-1</sup> with cycling stability to 112 cycles.

However, most inorganic catalysts randomly oxidize not only the discharge products but also the electrolyte and electrodes. Thus, the investigations on the cathode catalysts are the key to reduce the overpotential and to prevent the electrolyte/electrode decomposition in the Li-O<sub>2</sub> battery.<sup>9</sup>

## 1.2 High-Nickel Li[Ni,Co,Mn]O<sub>2</sub> Battery

The conventional lithium-ion battery (LIB) cathode was composed of the LiCoO<sub>2</sub> which demonstrates the specific capacity of 154 mAh g<sup>-1</sup>.<sup>10</sup> Yet, the expensive cost and toxicity of the cobalt raw materials have urged the development of the Ni-rich and Li-rich Li[Ni,Co,Mn]O<sub>2</sub> (NCM) layered oxide cathode materials.<sup>11</sup> Particularly, as the portion of the nickel increases, the specific capacity of the NCM increases beyond 200 mAh g<sup>-1</sup>.<sup>12</sup>

However, the commercialization of high-Ni NCM battery has been hindered because of poor capacity retention, low thermal stability and moisture/air sensitivity.<sup>13</sup> The major causes of those drawbacks are pointed out as 1) phase transformation from layered to spinel/rock-salt structure owing to nickel and lithium cation mixing<sup>14</sup> 2) side reaction with electrolyte resulting in thick cathode electrolyte interface (CEI) insulating layer<sup>15</sup> 3) micro-crack generation from repeated volume expansion/contraction<sup>16</sup> 4) transition metal dissolution by HF attack and release of oxygen as degradation of layered structure.<sup>17</sup>

Thus, extensive studies were performed to protect the surface of the NCM and/or enhance electronic/ionic conductivity through surface coating with inorganic insulators and/or conductive polymers.<sup>18</sup> So far, the inorganic materials such as Al<sub>2</sub>O<sub>3</sub>, SiO<sub>2</sub> and AlF<sub>3</sub> were profoundly utilized as the NCM coating layer.<sup>19</sup> Dong et al. reported Al<sub>2</sub>O<sub>3</sub> coated NCM811 under CO<sub>2</sub> flow and exhibited superior capacity retention and rate capability.<sup>20</sup> The 1wt% Al<sub>2</sub>O<sub>3</sub> coating retained 99% of its discharge capacity after 60 cycles at a cutoff voltage of 4.5 V. 115 Woo et al. showed the excellent cycle life, rate capability and thermal stability of AlF<sub>3</sub> coated NCM811.<sup>21</sup> The AlF<sub>3</sub> coating reduced the charge transfer resistance and protected the surface of NCM811 from side reaction with electrolyte.

However, since those inorganic materials lack the electronic conductivity, conductive polymers such as PEDOT, polypyrrole were widely investigated to improve the electronic and ionic conductivity of the coating layer.<sup>22</sup> Xu et al.

developed PEDOT coated NCM using chemical vapour deposition (CVD).<sup>23</sup> Their CVD method enabled uniform coating of secondary particles as well as primary particles and exhibited excellent cycle life at high cut off voltage.

Yet, the thickness control without disturbing the electronic/ionic conductivity remains as major issues. Thus, the development of the cathode coating material and methods are crucial in enhancing battery performance.

## 1.3 Cathode | Electrolyte Interface Engineering in Battery

The side reactions at the interface of cathode and electrolyte such as electrolyte decomposition, irreversible by-product generation, transition metal dissolution, cathode decomposition and phase transition inhibit the cycle performance in lithium batteries. Particularly, in lithium-air battery, the air cathode is known to determine the overall cell potential and capacity; while the potential of the lithium metal anode remain constant at a constant current, the overall cell potential dropped along with the potential of the air cathode.<sup>24</sup> Because major drop of the cathode performance was at the cathode/electrolyte interface, the interface engineering to control the cathode/electrolyte reaction is crucial in cell design. In this thesis, the cathode/electrolyte interface was engineered with catalysts (Chapter 2) and cathode coating (Chapter 3).

In chapter 2, the cathode/electrolyte interface of the Li-O<sub>2</sub> battery was modified with the cathode catalyst. The cathodic reaction of the Li-O<sub>2</sub> battery varied as the molecular structure of heme catalysts and its effect was evaluated with DFT calculations.

In chapter 3, the high-Ni NCM cathode materials in Li-ion battery was treated with organic coating layer to protect the surface from the unwanted side-reaction with electrolyte.

This thesis on the cathode/electrolyte engineering strategies would provide a logical designing methods to improve cathodic reaction in the energy storage systems.

# Chapter 2. Lewis Acidity Controlled Heme Catalyst for Lithium-Oxygen Battery

## 2.1 Introduction

Rechargeable lithium-oxygen (Li–O<sub>2</sub>) batteries have attracted a great deal of attention from the battery community, especially for the purpose of extending the driving mileage of electric vehicles (EVs), owing to their high theoretical specific energy of 3458 W h kg<sup>-1</sup>.<sup>25-30</sup> This large theoretical specific capacity stems from the use of oxygen gas in contrast to classical lithium-ion batteries (LIBs) that adopt solid-state electrodes on both sides that operate based on intercalation reactions.<sup>31-34</sup>

Although the extraordinary theoretical energy density is attractive, the cycle life of Li–O<sub>2</sub> batteries is below acceptable standards for practical use, the origin of which lies with a sluggish charging process.<sup>32, 35-41</sup> In practice, this is reflected in large overpotentials.<sup>41-46</sup> Hence, significant research efforts have been devoted to lower the charging overpotential, and development of oxygen evolution reaction (OER) heterogeneous catalysts such as metal oxide<sup>47-55</sup> and metal nanoparticles<sup>56-59</sup> is most representative in this direction.

Albeit the consensus on the importance of OER catalysts, the degree of charging overpotential varies substantially depending on material choice<sup>48, 53, 55, 57-59</sup> and interface plane.<sup>60</sup> It was found<sup>60-66</sup> that the adsorption strength of Li and O to the catalyst affects the (de)composition kinetics of discharged products and consequently the (dis)charging overpotential. Based on these studies, weak oxygen desorption energy from the surface of a catalyst has been desired for a facile charging process.<sup>60, 65, 66</sup> On the other hand, the discharge process inevitably yields superoxide radicals, which could indiscriminately attack the air electrode and produce irreversible side-products (i.e., Li<sub>2</sub>CO<sub>3</sub> formation upon attacking the

carbon electrode).<sup>37</sup> Hence, scavenging excessive superoxide radicals could be beneficial in protecting the air electrode and long term cycling.

Hemoglobin in red blood cells is known to deliver oxygen to tissues. Each hemoglobin consists of four hemes, which are responsible for oxygen delivery by binding and releasing oxygen molecules in response to surrounding oxygen partial pressure. Furthermore, heme scavenges reactive oxygen radical species (ROS) and protects the tissue from ROS attack.<sup>67, 68</sup> This well-known process in the human body hints at electrode design for Li–O<sub>2</sub> batteries, as ROS attack is one of the well-known causes for degrading the electrode and electrolyte.<sup>69</sup> Therefore, we conceptualize that hemoglobin-mimetic catalysts could prevent indiscriminate ROS attack by providing selective ROS binding sites and consequently improve the discharge-charge reversibility. Simultaneously, as addressed above, a proper level of binding affinity of oxygen (or oxygen intermediates) with the electrode surface is crucial for the facile progression of the reaction. This rationale led us to note that Lewis acidity could serve as a key parameter in realizing an appropriate strength of oxygen binding by inducing a certain degree of electron transfer from the oxygen molecule to a catalyst.<sup>66</sup> Having recognized the useful role of hemoglobin and Lewis acidity, herein, we have developed ligand-modified heme catalysts for air-cathodes in Li–O<sub>2</sub> batteries. A systematic investigation employing electron-withdrawing functional groups elucidates the importance of Lewis acidity. This function results in significantly decreased overpotentials and enhanced cycle life, offering a useful insight in catalyst design for air-cathodes.

## 2.2 Experimental

### 2.2.1 Synthesis of Heme, Heme+NCS and Heme+N<sub>3</sub> Catalysts

The bare Heme catalyst was prepared by dissolving 0.7 mM of hemin (from bovine >90%, Aldrich, USA) in ethyl alcohol (EtOH, Daejung, Korea):DI water (1:1 v/v) for 10 min. The catalyst was collected by using micro-centrifuge at 13500 rpm for 2 min, followed by washing with 1 mL of EtOH/DI water mixture (vol 1/1) three times. The collected catalyst was vacuum-dried at 25 °C overnight.

The Heme+N<sub>3</sub> and Heme+NCS catalysts were prepared by ligand exchange of the chloride group of hemin with azide and thiocyanate groups, respectively. 1 mL of 0.7 mM of hemin in EtOH was mixed with 1 mL of 0.7 mM sodium azide (NaN<sub>3</sub>, Aldrich, USA) or sodium thiocyanate (NaNCS, Aldrich, USA) in a solvent mixture (EtOH:DI water = 1:1= v:v). Both ligand-exchange reactions proceeded for 10 min with vigorous stirring. The catalysts were centrifuged *via* micro-centrifuge at 13500 rpm for 2 min, followed by washing with 1 mL of EtOH/DI water mixture (vol 1/1) three times to remove residual ions and drying under vacuum at 25 °C overnight.

### 2.2.2 Nitroblue Tetrazolium (NBT) Reduction Test

The nitroblue tetrazolium (NBT) reduction test was performed to evaluate the superoxide radical scavenging capability of the Heme, Heme+NCS and Heme+N<sub>3</sub> catalysts. 7.1 mg of potassium dioxide (KO<sub>2</sub>, Aldrich, USA) and 26.5 mg of 18-crown-6 (C<sub>12</sub>H<sub>24</sub>O<sub>6</sub>, Aldrich, USA) were dissolved in 1 mL of 0.05 M lithium bis(trifluoromethanesulfonyl) (LiTFSI, Aldrich, USA) in tetraethylene glycol dimethyl ether (TEGDME, Aldrich, USA). After 12 hours of stirring with light blockage, the unreacted reactants were precipitated, and the supernatant was used as the initial radical solution in the ROS scavenging test with the heme

derivatives. Before this test, the linear relation between radical concentration and NBT absorption was established. The initial radical solution was diluted with the electrolyte to prepare solutions diluted by factors of 1, 0.75, 0.5, and 0.25, respectively. 400  $\mu\text{L}$  of 500  $\mu\text{M}$  NBT (TCI, Japan) in 0.05 M LiTFSI/TEGDME was added to 1 mL of each solution. After 10 min of stabilization, UV-vis analysis was performed to compare the absorption at 560 nm. Next, 0.5 wt% of Heme, Heme+NCS and Heme+N<sub>3</sub> catalysts were added to 1 mL of the radical solution and vortexed for even dispersion. After 10 min, 400  $\mu\text{L}$  of 500  $\mu\text{M}$  NBT was mixed with 1 mL of each solution. The supernatant of each solution was collected by centrifuge at 13500 rpm for 10 min. The reduced NBT in each supernatant solution was subjected to UV-vis analysis at 560 nm (Perkin-Elmer, USA).

### **2.2.3 Characterization of Heme, Heme+NCS and Heme+N<sub>3</sub>**

To confirm the ligand exchange of the Heme, Heme+NCS and Heme+N<sub>3</sub> catalysts, Fourier-Transform Infrared (FTIR) (Perkin-Elmer, USA) analysis was carried out. In this analysis, the catalysts were pelletized with potassium bromide (KBr, Daejung, Korea) and measured in the range of 500–4000  $\text{cm}^{-1}$ . The morphological changes of air-cathodes and lithium metal anodes were examined by field-emission scanning electronic microscopy (FE-SEM) (Auriga, Carl Zeiss), and their crystal structures were characterized by X-ray diffraction analysis (SmartLab, Rigaku). The chemical compositions and bonding character of catalysts and discharge products were analyzed using X-ray photoelectron spectroscopy (XPS) (KBSI, Korea) with a photon source of Al-K $\alpha$  with 1486.6 eV. The C 1s peak was calibrated at 284.8 eV.

## 2.2.4 Li–O<sub>2</sub> Battery Preparation and Electrochemical Measurements

The air-cathodes were prepared by spray-coating a catalyst ink (catalyst:super P = 9:1 = w:w in ethanol) on the porous carbon paper coated with a gas diffusion layer (GDL) (SGL carbon). After vacuum-drying at 25 °C overnight, the catalyst-coated carbon paper was punched into disks with 10 mm in diameter. The mass loading of the catalysts was 0.5 mg cm<sup>-2</sup>. Swagelok-type cells were prepared by assembling a lithium metal anode, a glass fiber separator (Whatman, UK) impregnated with 100 μL of the electrolyte (1 M LiTFSI in TEGDME), and an air-cathode. The assembled cells were positioned in a glass chamber and purged with oxygen for 1 hour before measurements. The electrochemical performance of each cell was tested by galvanostatic measurements using a battery cycler (WonATech, WBCS3000, Korea). The galvanostatic measurements were performed by fixing the specific capacity at 500 or 1000 mAh g<sup>-1</sup> with a current density of 100 or 250 mA g<sup>-1</sup>. The cyclic voltammetry was performed in the voltage range of 2.2–4.5 V vs Li/Li<sup>+</sup> at a scan rate of 10 mV s<sup>-1</sup>.

## 2.2.5. Computational Details

Density functional theory (DFT) calculations were performed with the B3LYP/6–31G(d) functional/basis set combination using the Gaussian 16 program. The electrostatic potential maps were generated after the optimization of the molecular structures using the GaussView. Consistent color scaling and isovalues (0.05) were applied to each ESP map.

The desorption energy of each charging step was calculated based on the following relation:

$$\Delta E = (E_{\text{tot}} + nE_{\text{Li}} + mE_{\text{O}_2}) - E_{\text{Li}_x\text{O}_y^* \text{catalyst}}$$

Where  $E_{\text{tot}}$  is the total energy of the system,  $E_{\text{Li}}$  and  $E_{\text{O}_2}$  are the total energy of

isolated lithium and oxygen,  $n$  is the number of desorbed Li atoms,  $m$  is the number of desorbed oxygen molecule, and  $E_{\text{Li}_x\text{O}_y^*\text{catalyst}}$  is the total energy of substrate ( $\text{Li}_2\text{O}_2$ ,  $\text{LiO}_2$ ,  $\text{O}_2$ ) adsorbed on the catalyst.

## 2.3 Results and Discussion

### 2.3.1 Characterization of Heme Catalysts

In an attempt to observe the ligand effects of heme catalysts with different electronegativities, azide ( $\text{N}_3$ ,  $\text{N}-\text{N}\equiv\text{N}$ ) and thiocyanate (NCS,  $\text{S}-\text{C}\equiv\text{N}$ ) ligands were selected. The  $\text{N}_3^-$ - and NCS-coordinated heme is denoted as Heme+ $\text{N}_3$  and Heme+NCS, respectively, and were synthesized by ligand exchange of the chloride ligand in the hemin (Fig. 2.1a–c). The ligand complexation was confirmed by FTIR analysis (Fig. 2.1d); the  $\text{N}_3$  peak coordinated to heme was observed at  $2053\text{ cm}^{-1}$ , which is distinct from the unbound  $\text{N}_3$  peak that usually appears at  $2038\text{ cm}^{-1}$ .<sup>70</sup> The peak of Heme+NCS at  $2034\text{ cm}^{-1}$  was assigned to the vibration of  $\text{C}=\text{N}$  bonds in the NCS. Also, the  $\text{C}=\text{O}$  bond in the carboxylic acid group at the end of heme branches was reflected in the peak at  $1702\text{ cm}^{-1}$ .<sup>70-72</sup> As displayed in Fig. 2.2, the FTIR profiles of Heme+ $\text{N}_3$  before and after washing were completely different as unbound  $\text{N}_3$  species were washed away during the washing process.

Prior to the application of Heme, Heme+NCS, and Heme+ $\text{N}_3$  as cathode catalysts for  $\text{Li}-\text{O}_2$  batteries, their oxygen binding abilities were evaluated by the NBT reduction method (Fig. 2.1e).<sup>73,74</sup> This test is based on the fact that once superoxide radicals are generated *via* reaction between potassium superoxide ( $\text{KO}_2$ ) and crown ether, the generated superoxide radicals can be captured by the heme catalyst, with other residual superoxide radicals being scavenged by NBT. The amount of the consumed NBT can be detected<sup>73,74</sup> by monitoring the peak intensity at  $560\text{ nm}$  in UV-vis analysis. The quantitative correlation between NBT absorption and radical concentration was confirmed by a separate reference test (Fig. 2.3). At a fixed amount (0.5 wt%) of catalyst, all three heme derivative catalysts exhibited negligible absorption at  $560\text{ nm}$ , indicating that they all have the capability of scavenging oxygen radicals.

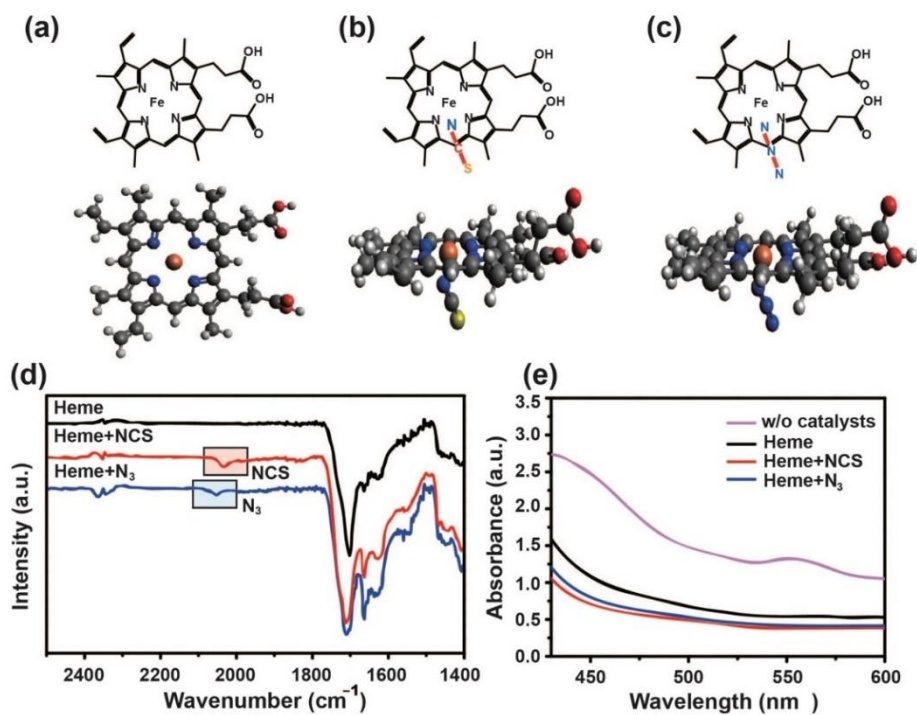


**Figure 2.1** Atomic configurations of (a) Heme, (b) Heme+NCS, and (c) Heme+N<sub>3</sub>. (d) FTIR spectra of the three samples. (e) UV-vis spectra showing NBT reduction by superoxide radical scavenging.

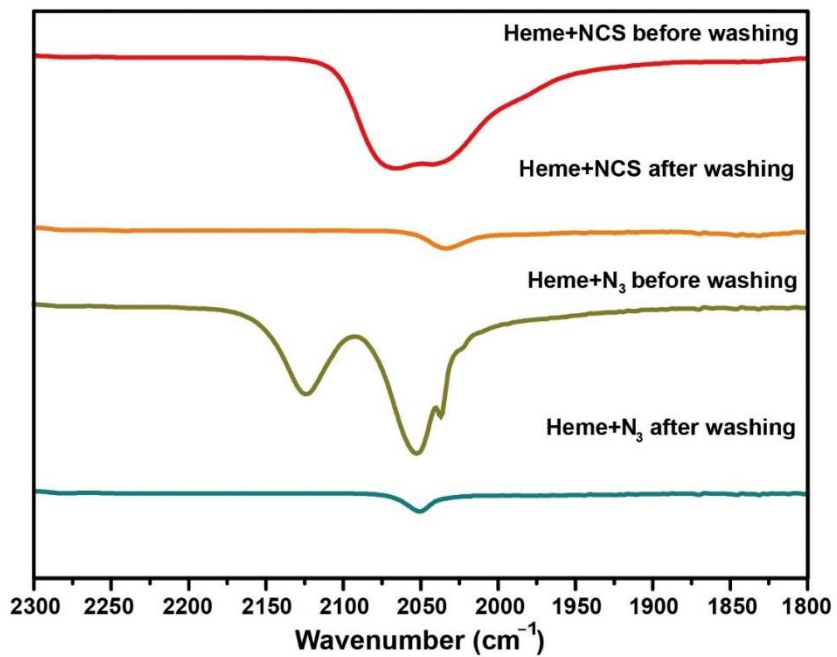


**Figure 2.2** FTIR profiles of Heme+NCS and Heme+N<sub>3</sub> before and after a washing process during synthesis.

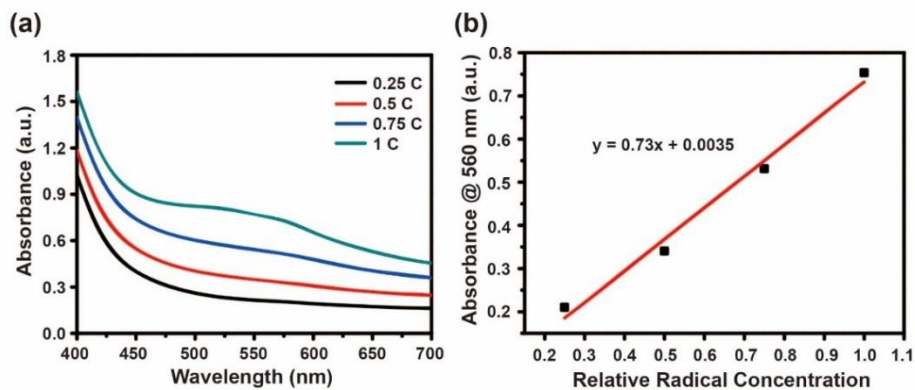


**Figure 2.3** (a) UV-vis absorbance of NBT at relative radical concentrations of 0.25 C, 0.5 C, 0.75 C and 1 C. 1 C is the concentration of the initial radical solution. (b) Correlation of NBT absorbance at 560 nm with the relative radical concentration.

## 2.3.2 Electrochemical Performance

In an effort to observe the ligand effect on the electrochemical performance of air-cathodes, the heme catalysts were spray-coated on a porous carbon paper. Once again, we focused on the electron donating/withdrawing effect of coordinated ligands during discharge so that the efficiency in the subsequent charging process would be affected. For this test, Li–O<sub>2</sub> cells were prepared in a Swagelok-type cell configuration in which lithium metal anodes and the aforementioned air-cathodes were assembled with the electrolyte, 1 M LiTFSI in TEGDME. The discharge-charge scan was galvanostatically swept between 2.2 and 4.5 V vs Li/Li<sup>+</sup> at a current density of 100 mA g<sub>carbon</sub><sup>-1</sup> (Fig. 2.4a). Notably, the ligand-coordinated Heme catalysts exhibited significantly reduced overpotentials during charging as compared to those of the bare Heme catalyst. At a specific capacity of 300 mAh g<sup>-1</sup>, the bare Heme catalyst showed a charge overpotential of ~0.83 V, whereas the overpotentials of the Heme+N<sub>3</sub> and Heme+NCS were ~0.72 and ~0.63 V, respectively.

The ligand effect on the charging efficiency was further investigated using cyclic voltammetry (CV) analysis (Fig. 2.4b). According to the CV profiles upon oxygen gas purging, the Fe<sup>3+</sup> in the heme was reduced to Fe<sup>2+</sup> at E<sub>c,1</sub> and oxidized at E<sub>a,2</sub>, returning to its initial oxidation state. The CV profiles were sustained over cycling, implying the decent reversibility of the catalysts (Fig. 2.5). The peaks originating from Li<sub>2</sub>O<sub>2</sub> oxidation (E<sub>a,1</sub>) and Fe<sup>2+</sup> oxidation peak (E<sub>a,2</sub>) indicate smaller overpotentials for Heme+NCS and Heme+N<sub>3</sub> as compared to those of bare Heme. The E<sub>a,1</sub> peaks of Heme, Heme+NCS, and Heme+N<sub>3</sub> were located at 3.66, 3.60 and 3.63 V, respectively (Fig. 2.4c). Similarly, the E<sub>a,2</sub> peaks of the same three samples were located at 4.38, 4.33, and 4.31 V, respectively (Fig. 2.4d). The lowered overpotentials of Heme+NCS and Heme+N<sub>3</sub> reconfirm the role of the ligand coordination in improving the charging kinetics by providing Lewis acidic active sites. Although the elucidation of the distinct overpotentials between

Heme+NCS and Heme+N<sub>3</sub> requires further investigation, it is anticipated that the higher Lewis acidity of Heme+NCS facilitates the discharging process *via* lowered desorption energies of reaction intermediates, as will be discussed later in this paper.

The distinct overpotentials among the samples were translated to the cycling performance. When the specific capacity was fixed at 500 mAh g<sup>-1</sup>, the three cells showed distinct performance levels when measured at 100 and 250 mA g<sup>-1</sup> (Fig. 2.6a and b). At 100 mA g<sup>-1</sup> (Fig. 2.6a), whereas the capacities of the bare Heme and Heme+N<sub>3</sub> cells dropped abruptly at the 70<sup>th</sup> and 160<sup>th</sup> cycles, respectively, the Heme+NCS cell did not display such capacity drop over 225 cycles. The Heme+NCS cell maintained 88% of the original capacity after 200 cycles. It is conjectured that the sudden capacity drop of the Heme and Heme+N<sub>3</sub> cells is ascribed<sup>75, 76</sup> to the accumulation of the irreversible discharge products, such as Li<sub>2</sub>CO<sub>3</sub> and LiCOOR, as shown in the SEM and FTIR results in Fig. 2.7. When tested at 250 mA g<sup>-1</sup> (Fig. 2.6b), the cells exhibited a similar trend, although the capacity drop points were delayed to the 23<sup>rd</sup>, 42<sup>nd</sup> and 50<sup>th</sup> cycles, respectively. During cycling, the discharge/charge profiles showed negligible changes at both 100 and 250 mA g<sup>-1</sup> as shown in Fig. 2.8. Also, the discharge-charge reversibility was examined with focus on the morphology of discharge products using SEM analysis after 1<sup>st</sup> discharge and charge. For all of the three electrodes, the generated Li<sub>2</sub>O<sub>2</sub> during 1<sup>st</sup> discharge disappeared mostly after 1<sup>st</sup> charge (Fig. 2.9). However, the morphology change was quite similar among the samples. On the other hand, the enhanced cyclability of Heme+NCS was preserved when the fixed capacity was increased to 1000 mAh g<sup>-1</sup> (Fig. 2.10). Once again, the superior cyclability of the Heme+NCS cell is attributed to the enhanced catalytic effect on Li<sub>2</sub>O<sub>2</sub> decomposition, which is related to its low overpotentials during charge.

In order to elucidate the role of ligand coordination on the charge-discharge reversibility, XPS analyses were conducted for the three cells after 1<sup>st</sup> discharge (constrained to 250 mAh g<sup>-1</sup>), 10<sup>th</sup> discharge (constrained to 250 mAh g<sup>-1</sup>

fixed), and 1<sup>st</sup> full discharge. In the XPS data in Fig. 2.11, the C 1s spectra of all cells consistently showed peaks corresponding to ether/alkoxides (C–O), carboxylates (LiCOOR), and carbonates (Li<sub>2</sub>CO<sub>3</sub>) at 286.6, 288.8, and 289.8 eV, respectively. Nonetheless, the deconvolution of the profiles reveals that the Heme+NCS and Heme+N<sub>3</sub> catalysts exhibited smaller peaks at 286.3, 288.8 and 289.8 eV assigned to C–O, LiCOOR and Li<sub>2</sub>CO<sub>3</sub> at the same cycling states, implying that the production of the discharge products was lessened by the incorporation of the catalysts.

The morphology of discharge products and Li metal anodes was also examined. From the XRD spectra and SEM images of the air-cathodes after cycles, the morphology of the discharge products did not vary much with the catalysts incorporated (Fig. 2.12 and 2.13). In addition, according to the top-view and cross-section SEM images of the Li metal anodes (Fig. 2.14 a-f), their morphology after 10 cycles was not different significantly among the three electrode cases. Also, EDX analysis could not detect Fe on the lithium metal anodes after 10 cycles for all of the three electrodes (Fig. 2.14 g-i), implying that catalyst dissolution was not serious. Thus, the different lewis acidity did not largely affect the morphology of discharge products and lithium metal counter electrodes. Hence, it can be seen that the enhanced discharge-charge efficiency is due to the ligand-coordination to the heme catalysts, which results in weakened parasitic reactions at the air-cathodes.

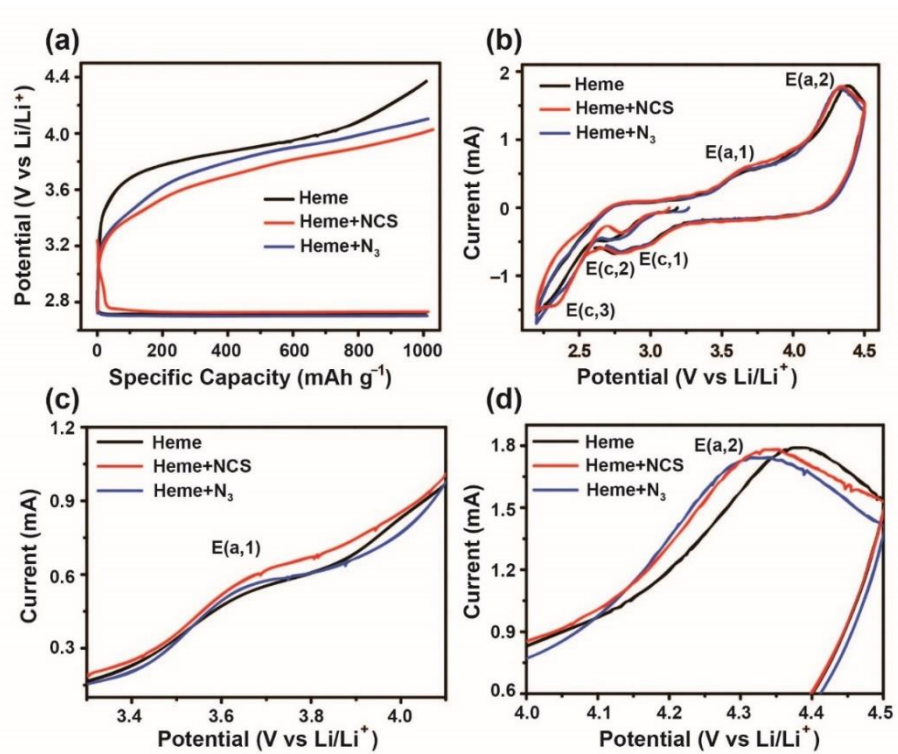


**Figure 2.4** (a) 1<sup>st</sup> discharge/charge profiles and (b) cyclic voltammetry curves in the potential range of 2.3 to 4.5 V at a scan rate of 0.1 mV s<sup>-1</sup>. Enlarged cyclic voltammetry profiles in the potential range of (c) 3.3~4.3 V and (d) 4.0~4.5 V for Heme, Heme+NCS, and Heme+N<sub>3</sub> electrodes.

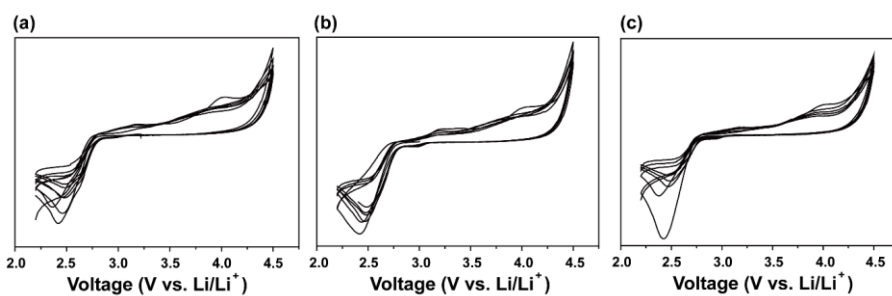


**Figure 2.5** Cyclic voltammetry profiles of (a) Heme, (b) Heme+NCS and (c) Heme+N<sub>3</sub> when scanned at 0.1 mV s<sup>-1</sup> for 5 cycles.

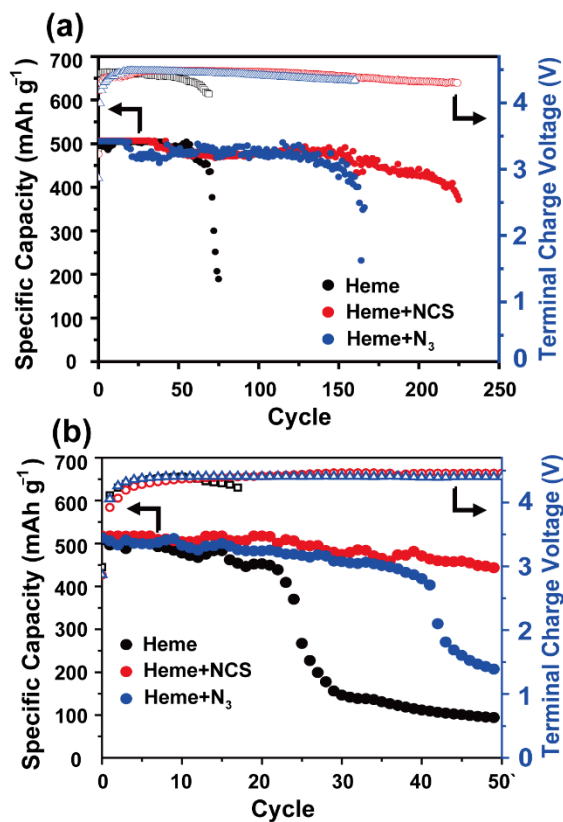


**Figure 2.6** Cycling performance with a fixed capacity of 500 mAh g<sup>-1</sup> at a current density of (a) 100 mA g<sup>-1</sup> and (b) 250 mA g<sup>-1</sup>, with the right y-axes indicating terminal charge voltage.

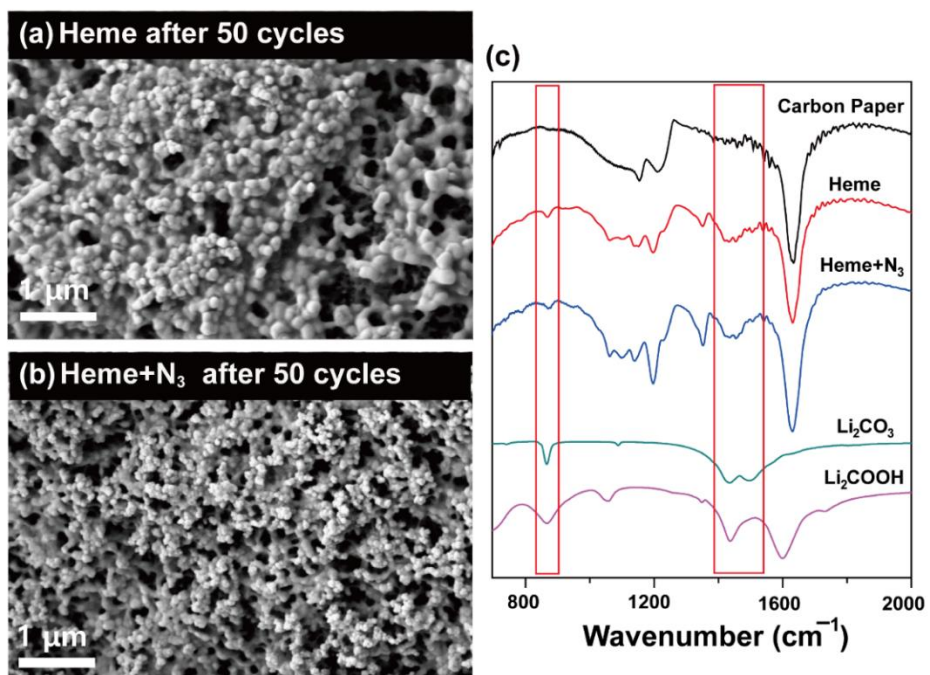


**Figure 2.7** (a,b) SEM and (c) FTIR results of Heme and Heme+N<sub>3</sub> air-cathodes after 50 cycles in Figure 2.6.

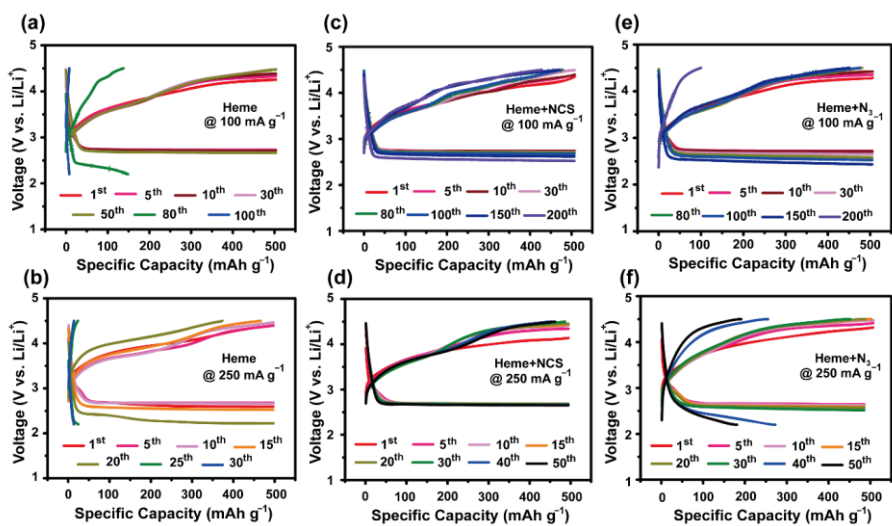


**Figure 2.8** Discharge-charge profiles of (a,b) Heme, (c,d) Heme+NCS, (e,f) Heme+N<sub>3</sub> at 100 and 250 mA g<sup>-1</sup>.

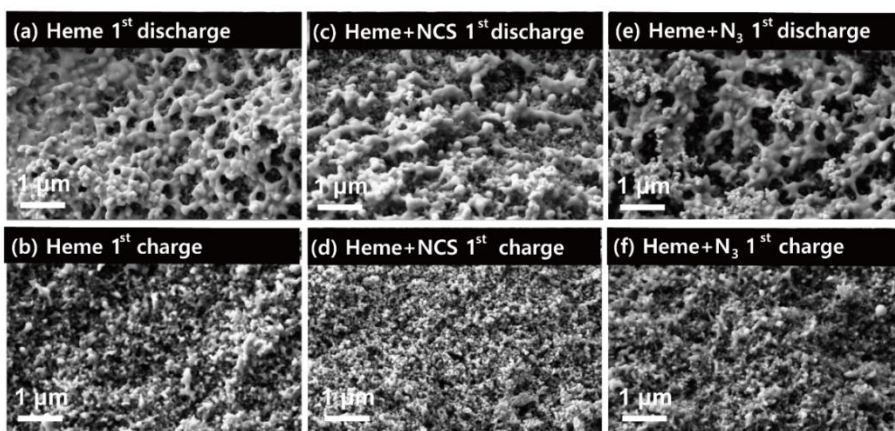


**Figure 2.9** SEM images of (a,b) Heme, (c,d) Heme+NCS and (e,f) Heme+N<sub>3</sub> air-cathodes after 1<sup>st</sup> discharge and 1<sup>st</sup> charge, respectively.

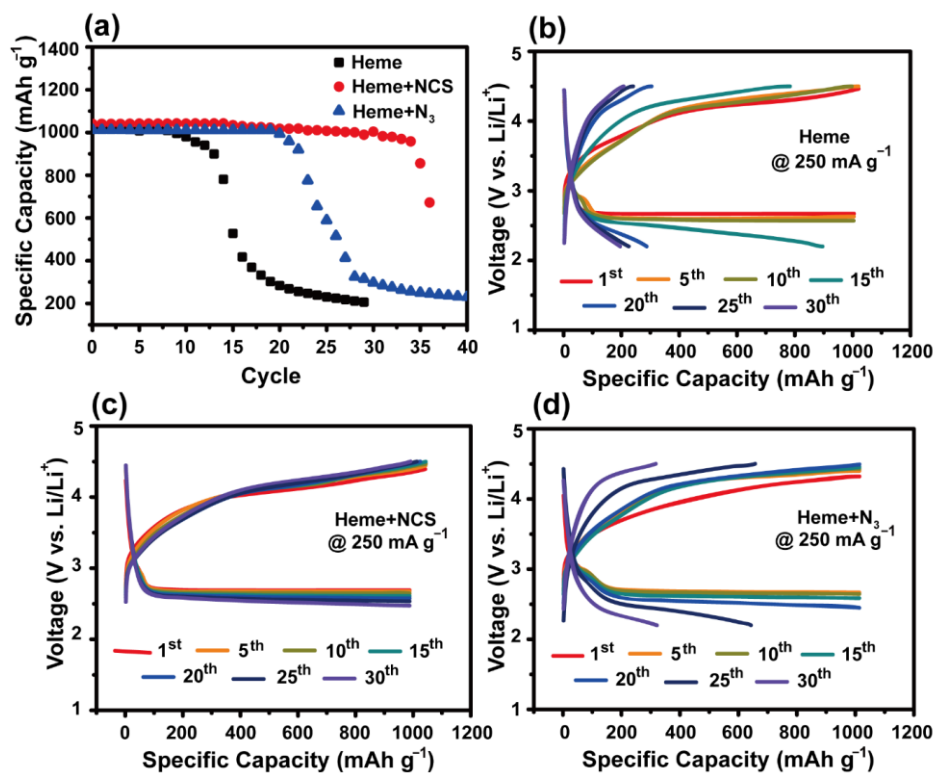


**Figure 2.10** (a) Cycling performance of Heme, Heme+NCS, and Heme+N<sub>3</sub> at 250 mA g<sup>-1</sup> with a fixed capacity of 1000 mAh g<sup>-1</sup> and (b-d) their respective discharge-charge profiles at different cycle numbers.

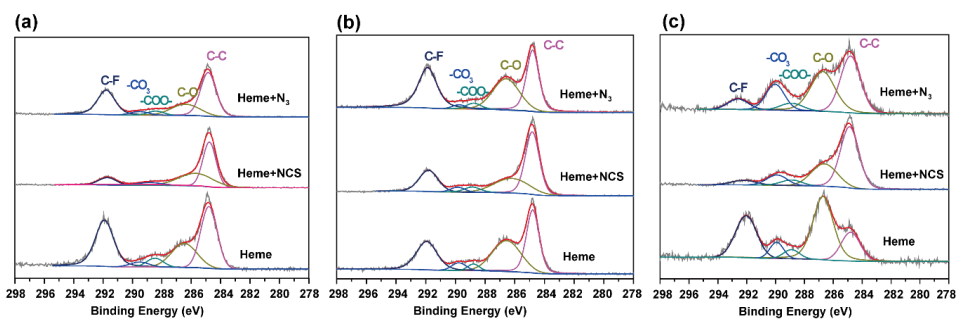


**Figure 2.11** XPS profiles of Heme, Heme+NCS and Heme+N<sub>3</sub> electrodes after (a) 1<sup>st</sup> discharge, (b) 10<sup>th</sup> discharge, and (c) 1<sup>st</sup> full discharge.

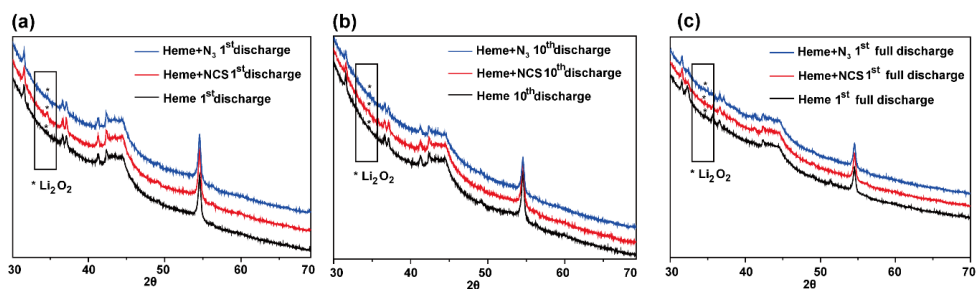


**Figure 2.12** XRD profiles of Heme, Heme+NCS and Heme+N<sub>3</sub> electrodes after (a) 1<sup>st</sup> discharge, (b) 10<sup>th</sup> discharge, and (c) 1<sup>st</sup> full discharge.

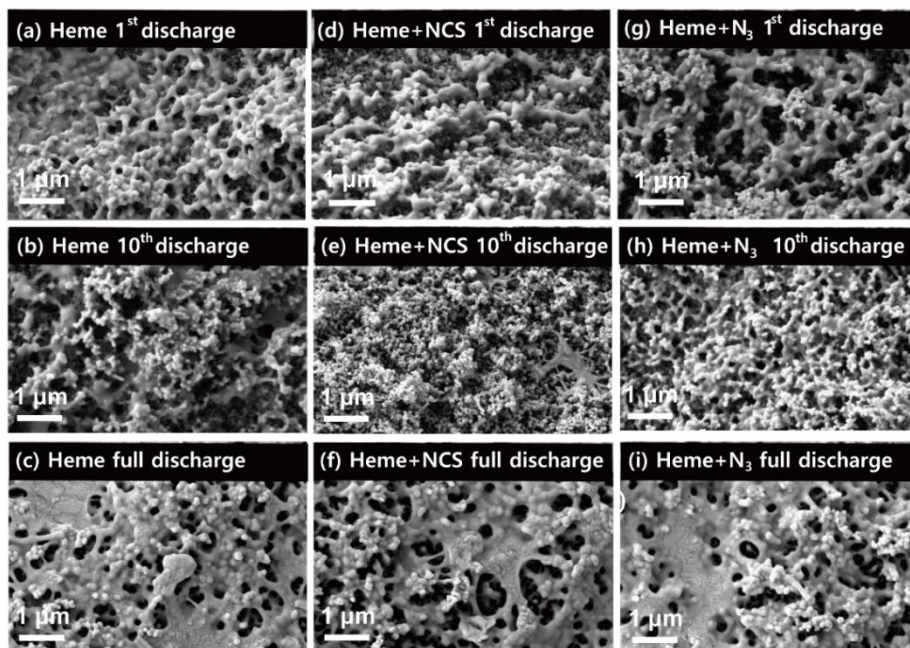


**Figure 2.13** SEM images of (a,b,c) Heme, (d,e,f) Heme+NCS, and (g,h,i) Heme+N<sub>3</sub> air-cathodes after 1<sup>st</sup> discharge, 10<sup>th</sup> discharge, and 1<sup>st</sup> full discharge, respectively.

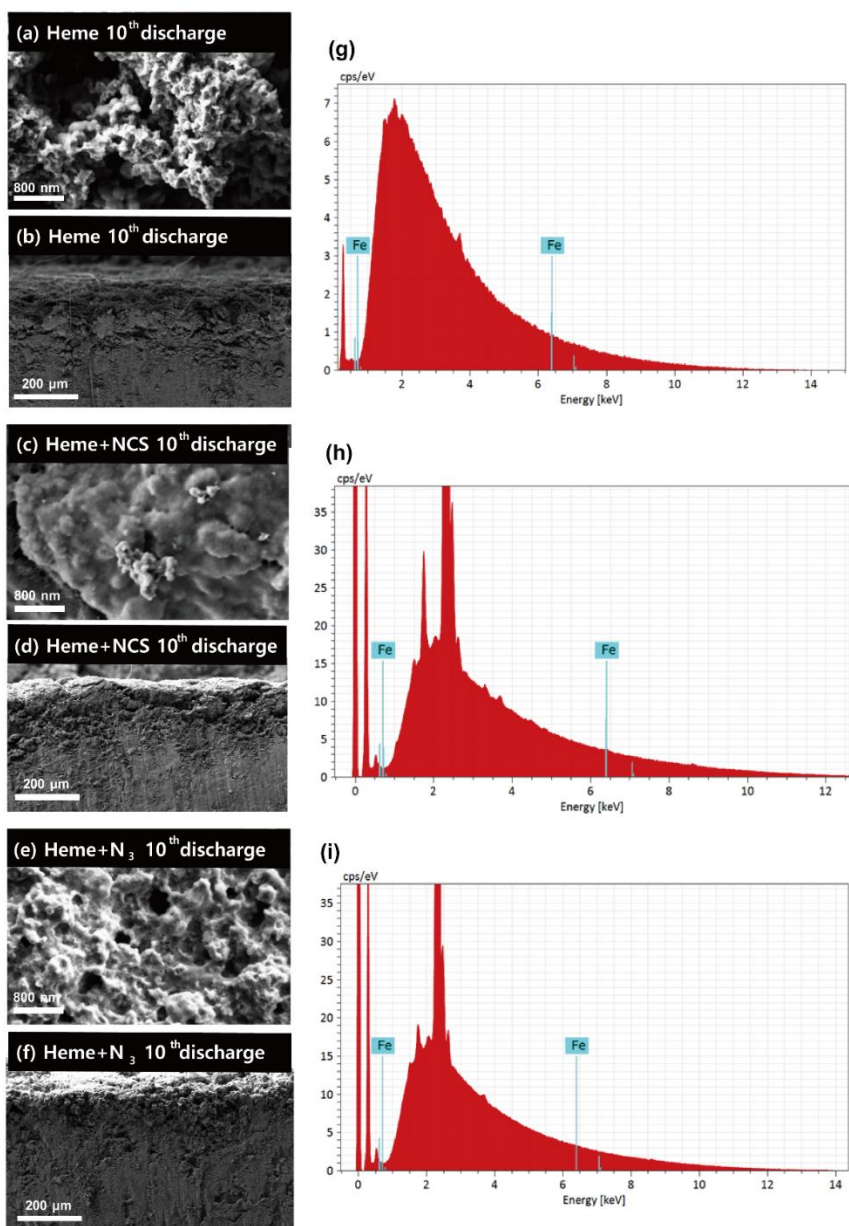


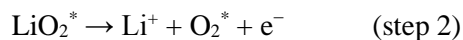
**Figure 2.14** The top-view and cross-section SEM images and EDX analysis of Li metal anodes after 10 cycles for (a,b,g) Heme, (c,d,h) Heme+NCS and (e,f,i) Heme+N<sub>3</sub> cathodes.

### 2.3.3 Density Functional Theory (DFT) Calculations

To unravel the origin of the enhanced catalytic effect of the ligand-modified catalysts, the electronic structures of each catalyst were scrutinized using DFT calculations. The electrostatic potential maps of the Heme, Heme+NCS, Heme+N<sub>3</sub> catalysts are presented in Fig. 2.15a–c. In these maps, red and blue colors indicate electron rich and deficient sites. Mulliken charge near the heme center and on the ligand was also calculated to see the charge distribution quantitatively. While the Mulliken charge of the Fe was 0.948 for Heme, that of Heme+NCS and Heme+N<sub>3</sub> was more positive to be 1.151 and 1.211, respectively. Similarly, the Mulliken charge of the nitrogen in the porphyrin ring changed in such a way that the values of the ligand-modified ones became less negative: –0.835 for Heme, –0.722 for Heme+NCS, and –0.745 for Heme+N<sub>3</sub>. The more positive Mulliken charge of the Fe centers in the ligand-modified species implies that the introduction of the thiocyanate and azide ligands with electron-withdrawing nature renders the catalytic centers more positively charged and induces higher Lewis acidity. The generation of more Lewis acidic active sites was further verified by XPS of the as-synthesized heme and ligand-attached heme analogues in the N 1s branch (Fig. 2.15d). The nitrogen peaks of Heme+NCS and Heme+N<sub>3</sub> relating to the porphyrin ring (pyridinic N) were both blue-shifted to 398.2 eV compared to that of bare Heme (397.5 eV), which is in good agreement with the change in the Mulliken charge; the charge became less negative upon ligand coordination. For reference, nitrogen in NCS and N<sub>3</sub> was observed at around 397.2 and 401.8 eV, respectively, (Fig. 2.16).<sup>79-81</sup> Unlike pyridinic N, the pyrrolic N at 399.8 eV did not shift because the pyrrolic N arose from unchelated porphyrin residues. In Fig. 2.17, the XPS spectra in Fe2p branch clearly showed the presence of Fe<sup>3+</sup> in all of Heme, Heme+N<sub>3</sub>, and Heme+NCS, as the spectra exhibited the Fe 2p<sub>3/2</sub> and Fe 2p<sub>1/2</sub> peaks at 710.8 and 724.1 eV, together with the satellite peaks at 716.7 and 728.5 eV. From these observations, in accordance with the prediction from DFT calculations, the

ligand modification did not change the oxidation state of the Fe of the heme structure drastically, but mainly induced lewis acidity as indicated by the blue-shift in the nitrogen branch. Importantly, the presence of more Lewis acidic active sites alters the binding affinity of reaction intermediates during the charging process in Li–O<sub>2</sub> batteries and could promote the Li<sub>2</sub>O<sub>2</sub> decomposition for an efficient charging process.

The effect of Lewis acidity in catalyzing reactions at the air-cathode was further investigated by focusing on each charging step *via* DFT calculations as shown in Fig. 2.18a and b. The charging process of Li–O<sub>2</sub> batteries can be divided into the following three steps:<sup>60, 64-66</sup>



where LiO<sub>2</sub><sup>\*</sup> and O<sub>2</sub><sup>\*</sup> denote adsorbed species on the active site of a catalyst.

In the first step, Li<sub>2</sub>O<sub>2</sub> is decomposed to Li<sup>+</sup> and LiO<sub>2</sub><sup>\*</sup>, which is further dissociated to Li<sup>+</sup> and O<sub>2</sub><sup>\*</sup> in the second step. In the third step, O<sub>2</sub><sup>\*</sup> is detached from the active site, and this reaction constitutes the rate-determining step (RDS) in the entire charging process.<sup>60, 65, 66</sup> According to our calculations, the oxygen desorption energy in step 3 decreases upon coordination with NCS and N<sub>3</sub> (Fig. 2.18a). It has been adopted<sup>82-85</sup> that the O<sub>2</sub><sup>\*</sup> binding to the active Fe site is based on the interaction between the non-bonding *d*-orbital of Fe and the anti-bonding π\* orbital of O<sub>2</sub><sup>\*</sup> (Fig. 2.18c). Thus, when electron-withdrawing ligands are attached to the Fe, the Fe–O<sub>2</sub><sup>\*</sup> bond strength would become weakened, leading to a lower O<sub>2</sub><sup>\*</sup> desorption energy. In addition, the lithium dissociation energy in step 2 decreased with ligand coordination, even though Δ*E* difference between the samples with and without the ligand coordination is far smaller compared to that in step 3. In step 2, the dissociation of LiO<sub>2</sub><sup>\*</sup> could be hindered by the electrostatic attraction between Li<sup>+</sup> in LiO<sub>2</sub><sup>\*</sup> and the electronegative surface atoms.<sup>66</sup> The Mulliken charge calculations indicate less negative charge of the nitrogen in the porphyrin ring for

Heme+NCS and Heme+N<sub>3</sub> (-0.782 and -0.815, respectively) compared to that of bare Heme (-0.851) (Fig. 2.19), suggesting their weaker electrostatic interaction with Li<sup>+</sup> and explaining the more efficient LiO<sub>2</sub><sup>\*</sup> dissociation of both ligand-coordinated samples. Hence, the Lewis acidity of Heme+NCS and Heme+N<sub>3</sub> plays a key role in enhancing the charging efficiency *via* weaker interaction of the reaction intermediates. As for the discharging reaction, the full discharge capacity increased with increasing Lewis acidity (Fig. 2.20), which could be explained by the weaker binding of LiO<sub>2</sub> and Li<sub>2</sub>O<sub>2</sub> during the discharging process that could drive the reaction toward Li<sub>2</sub>O<sub>2</sub> generation. More in-depth study is required for clear understanding. The trend that correlates the Mulliken charge of Fe with overpotential and desorption energy is summarized in Fig. 2.21.

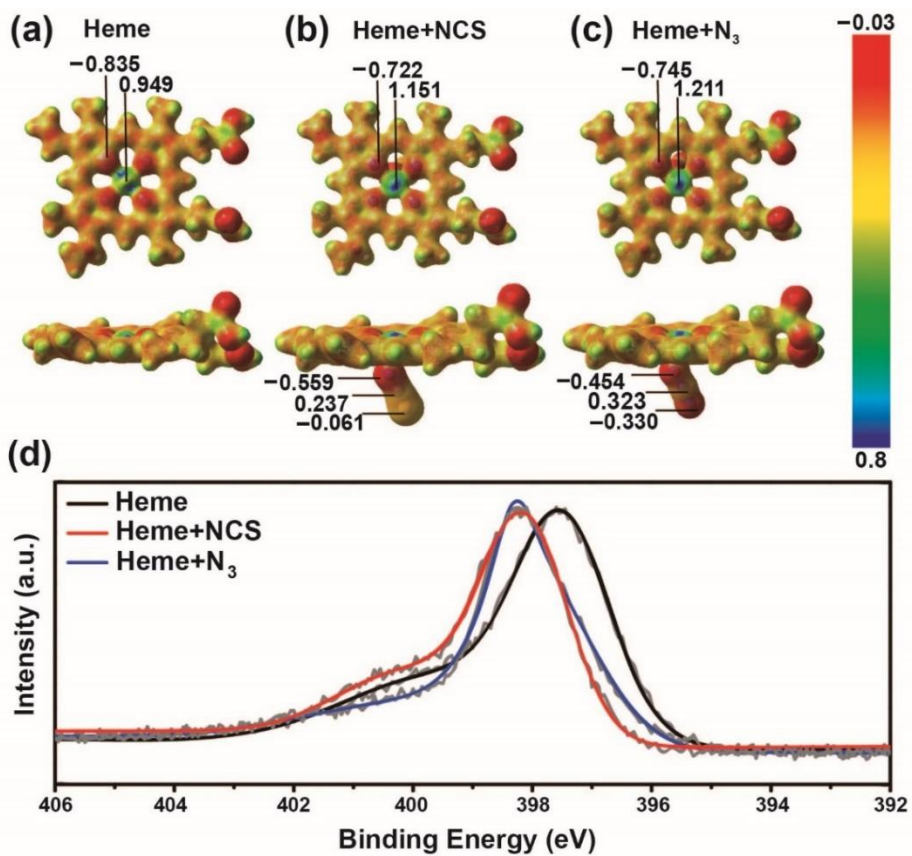


**Figure 2.15** Electrostatic potential map and Mulliken charge distributions of (a) Heme, (b) Heme+NCS, and (c) Heme+N<sub>3</sub>. (d) XPS spectra of the three samples at the N 1s branch.

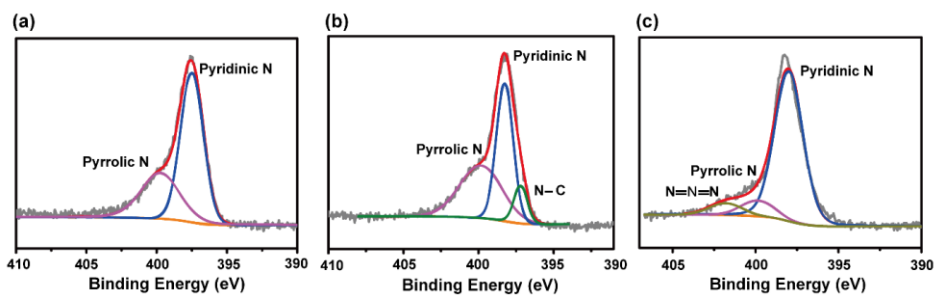


**Figure 2.16** XPS spectra of (a) Heme, (b) Heme+NCS and (c) Heme+N<sub>3</sub> in N 1s branch.

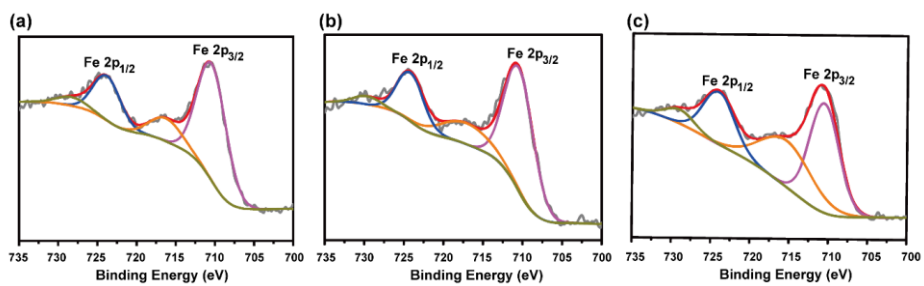


**Figure 2.17** XPS spectra of (a) Heme, (b) Heme+NCS and (c) Heme+N<sub>3</sub> in Fe 2p branch.

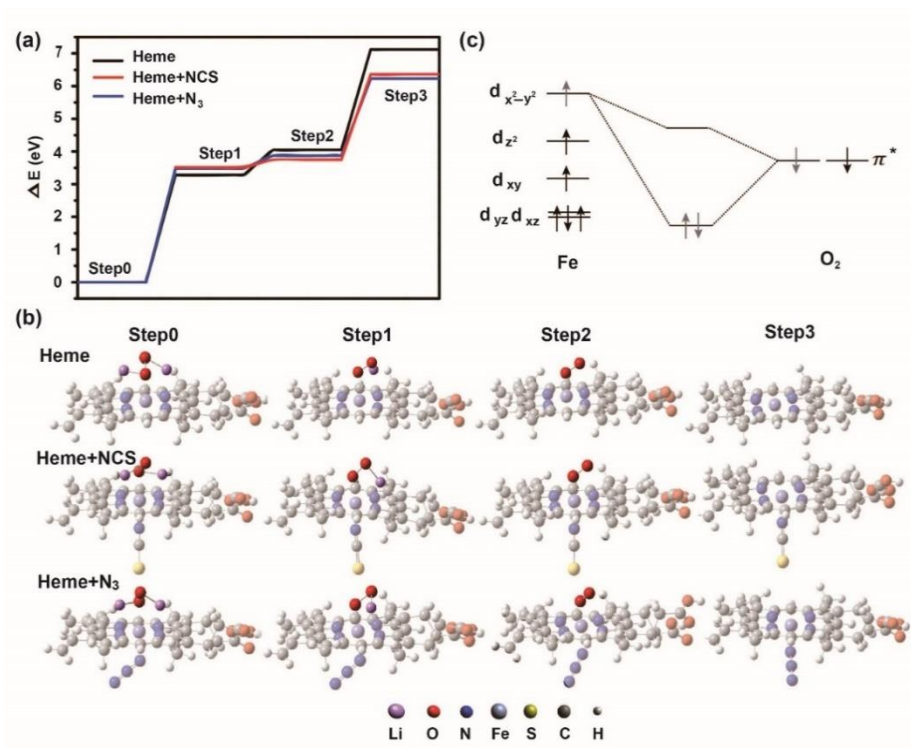


**Figure 2.18** (a) Energy profiles of Heme, Heme+NCS, and Heme+N<sub>3</sub> along the course of charging process. (b) Molecular structures of Heme, Heme+NCS and Heme+N<sub>3</sub> at each charging step. (c) Electron configuration of Fe-O<sub>2</sub> bond upon O<sub>2</sub> adsorption.

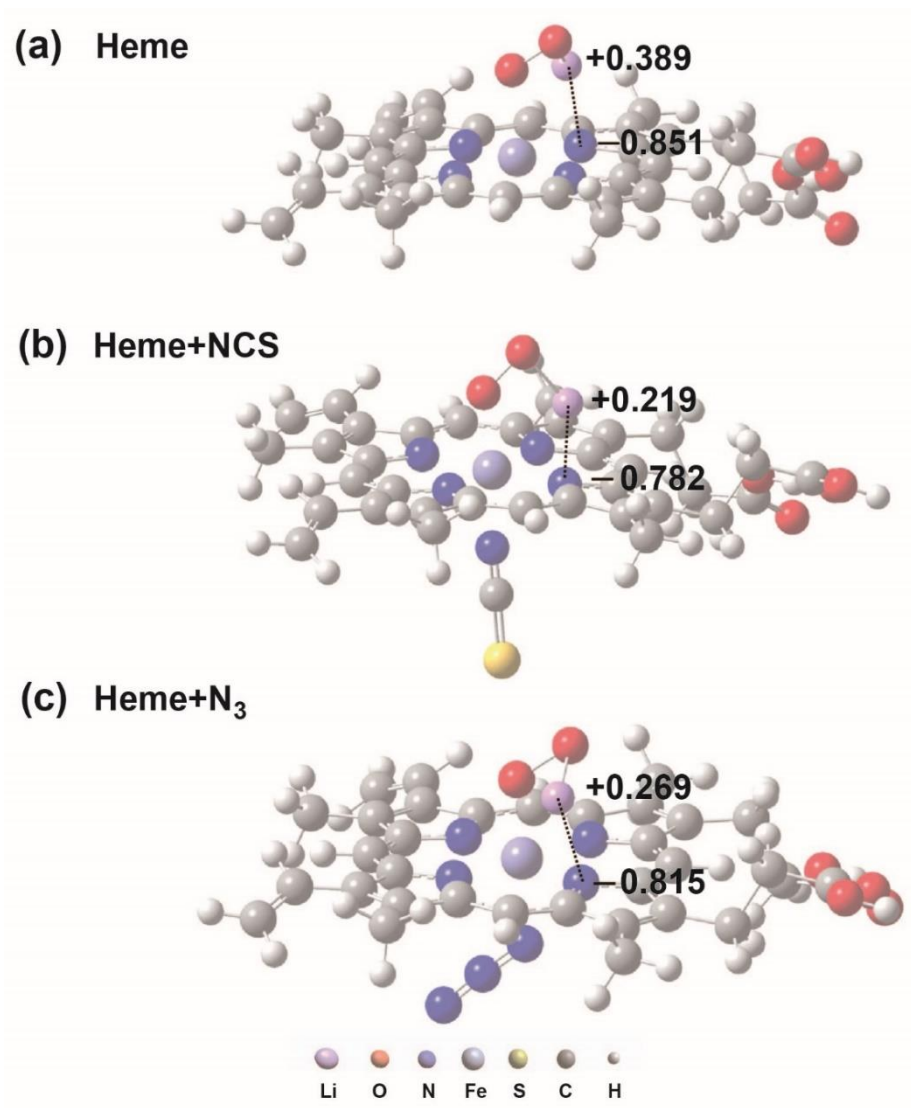


**Figure 2.19** Molecular structures of Heme, Heme+NCS and Heme+N<sub>3</sub> at the charging step 2. The mulliken charge of the Li<sup>+</sup> in LiO<sub>2</sub><sup>\*</sup> and the nitrogen in the porphyrin ring is denoted.

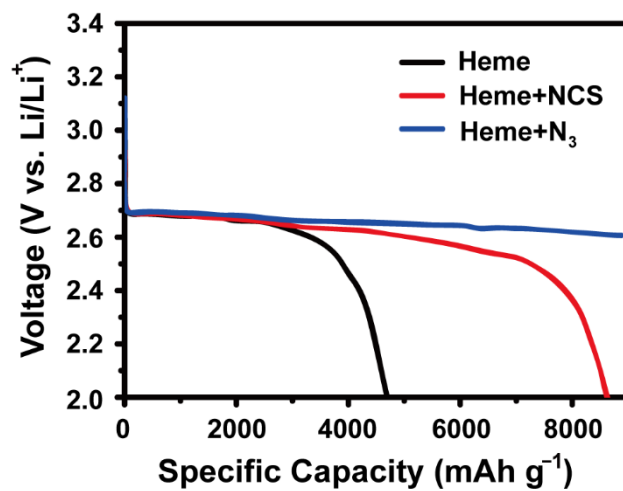


**Figure 2.20** Full discharge profiles of Heme, Heme+NCS and Heme+N<sub>3</sub> electrodes.

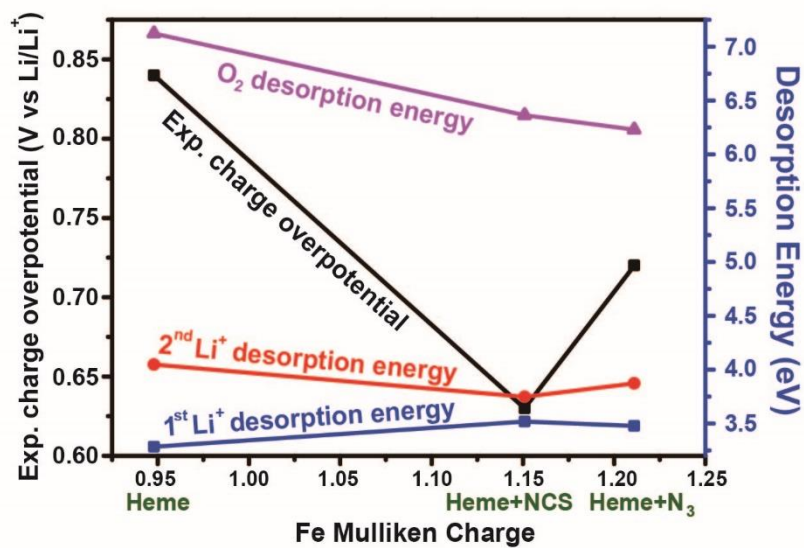


**Figure 2.21** Overpotentials and desorption energies of Heme, Heme+NCS and Heme+N<sub>3</sub> in correlation with the Mulliken charge of Fe.

## 2.3 Conclusion

The reversibility in each cycle is most critical in extending the cycle life of Li-O<sub>2</sub> batteries. Accordingly, the extent of Li<sub>2</sub>O<sub>2</sub> decomposition during the charge process is a key parameter. The Li<sub>2</sub>O<sub>2</sub> decomposition can be promoted by finding suitable catalysts in which the binding affinity of reaction intermediates with the active catalytic sites is optimized. Inspired by the functions of hemoglobin that carries oxygen molecules and scavenges ROS, we have adopted heme as a catalyst framework and further modified the electronic structure of its binding site by coordinating with NCS and N<sub>3</sub> ligands. The electron-withdrawing nature of these ligands weakens the binding strength of LiO<sub>2</sub>\* and O<sub>2</sub>\*, therefore lowering the activation barriers in the key reaction steps and consequently overpotentials. This investigation provides a useful guideline in designing air-cathode catalysts, that is, the electronegativity tuning of the active site of a catalyst that can scavenge oxygen molecules within its ring structure.

# Chapter 3. Pyrazine-linked 2D Covalent Organic Frameworks as Coating Material for High-Nickel Layered Oxide Cathodes in Lithium-Ion Batteries

## 3.1 Introduction

The emergence and steady growth of the electric vehicle market has demanded an improvement of various aspects of the performance of rechargeable lithium-ion batteries (LIBs).<sup>86-87</sup> Although the original cobalt (Co)-based layered oxide cathode, namely  $\text{LiCoO}_2$ , has been quite successful as a cathode material because of its advantageous stable structure, easy synthesis, and established electrolyte chemistry, the cost of raw cobalt-containing minerals has recently fluctuated, promoting research to reduce the Co content of these materials. Moreover, the continuous demand for high energy density has encouraged the adoption of nickel (Ni) as the main transition metal (TM) in the metal oxide structure because the Ni redox center in the layered oxygen framework offers large reversible capacity and chemical stability against oxygen loss, which is attributed to the small overlap between the  $\text{Ni}^{3+/4+}$   $e_g$  band and  $\text{O}^{2-}$   $2p$  band.<sup>88-90</sup> Indeed, the high-Ni  $\text{LiNi}_{0.8}\text{Co}_{0.1}\text{Mn}_{0.1}\text{O}_2$  composition (often referred to as NCM811) can increase the gravimetric capacity by approximately 40% as compared to that of its  $\text{LiCoO}_2$  counterpart ( $\sim 200$  vs.  $\sim 145$   $\text{mAh g}^{-1}$ ).<sup>91-95</sup>

Nevertheless, high-Ni NCM cathodes undergo serious degradation *via* several mechanisms.<sup>96-100</sup> The fact that  $\text{Ni}^{2+}$  and  $\text{Li}^+$  are similarly sized leads to so-called cation mixing during cycling, which can result in the well-known phase transition to the spinel and rock-salt phases. Cation mixing also promotes the dissolution of Ni or other TMs, which can destabilize the cathode-electrolyte interphase (CEI) by catalyzing unwanted reactions with the electrolyte.<sup>101-103</sup> These

degradation processes are accelerated at high temperatures, and therefore high-Ni NCM cathode materials are usually noted for their weak stability at elevated temperatures.<sup>104-105</sup> Moreover, repeated changes in the anisotropic volume give rise to the formation of micro-cracks,<sup>106-110</sup> which further induce side reactions on the surfaces of particles. Unfortunately, individual degradation processes often affect one another to ultimately accelerate the overall degradation. Attempts to avoid these detrimental degradation processes, which are typically initiated from the surface inward, led to the adoption of a variety of surface modifications. Along this direction, both inorganic<sup>111-112</sup> and polymeric<sup>113-114</sup> coating materials were investigated and were demonstrated to be effective in mitigating the aforementioned degradation processes to a certain extent. Of these two groups of materials, inorganic materials have been more widely studied, and diverse examples have been reported: Al<sub>2</sub>O<sub>3</sub>,<sup>115-116</sup> LiNbO<sub>3</sub>,<sup>117-118</sup> SiO<sub>2</sub>,<sup>119</sup> ZrO<sub>2</sub>,<sup>120</sup> TiO<sub>2</sub>,<sup>121</sup> AlPO<sub>4</sub><sup>122</sup> and AlF<sub>3</sub>.<sup>123</sup> Even though these ceramic and polymeric coating materials succeeded in improving the performance, most of these materials are electronic insulators, limiting the rate performance or the material loading in a given area. In an effort to overcome the limited electronic conductivity, conductive polymers such as PEDOT,<sup>113, 124-125</sup> PEDOT-*co*-PEG,<sup>126-127</sup> polyaniline,<sup>128</sup> and polypyrrole<sup>129-131</sup> were examined as materials for coating NCM. However, these polymers do not have any orientation when applied in the form of a coating such that a coating with a uniform thickness is often not warranted, leading to batch-to-batch deviation.

On the other hand, covalent organic frameworks (COFs) have received a great deal of attention from the various materials community because of their easy synthesis and their possible use for an extensive range of applications based on their low gravimetric densities and structural variability.<sup>132-134</sup> Furthermore, COFs can form periodically ordered molecular building blocks with regular pores and uniform distributions of elements.<sup>135-136</sup> Among the well-known COF units comprising characteristic chemical bonds<sup>137</sup> including B–O, C=N, C≡N, C–N, B=N and N=N, pyrazine, which contains two nitrogen atoms in its aromatic ring,

can be a useful component for coating NCM materials. This is because the 2D planar morphology of its linked COFs can be aligned along the surface of an NCM particle.<sup>138</sup> Moreover, the conjugated bond configuration of COFs enables high electronic conductivity, while their rigid porous structures that contain nitrogen with a lone pair of electrons can promote ionic transport.<sup>139-140</sup>

In this study, the use of a pyrazine-linked 2D sheet (denoted Pyr-2D) was investigated as a protective coating material for high-Ni NCM cathodes as this approach would take advantage of the planar morphology and conjugated bond configuration of pyrazine. Upon coating with Pyr-2D, NCM811 electrodes significantly improved their rate capability, cycling performance, and tolerance of high temperatures. The electrochemical results of the Pyr-2D-coated electrodes demonstrate the effective protection of NCM811 from undesired side reactions and inevitable attack by hydrofluoric acid (HF). The improved performance is attributed to the central role of the 2D morphology and conjugated atomic configuration of Pyr-2D, highlighting the great potential of 2D conjugated polymers as coating materials for emerging electrode materials for batteries.

## 3.2 Experimental

### 3.2.1 Synthesis of the Materials

The 2D sheet consisting of linked pyrazine units was coated onto Ni-rich NCM by the condensation reaction of amine and ketone in the presence of NCM811 particles. More specifically, 0.1 mmol benzenetetramine hydrochloride (Sigma-Aldrich, USA), 0.1 mmol of triquinoyl hydrate (TCI, Japan), and 1 g of  $\text{LiNi}_{0.8}\text{Co}_{0.1}\text{Mn}_{0.1}\text{O}_2$  (LNF, Korea) were dissolved in 10 mL *N*-methyl pyrrolidone (NMP, Junsei, Japan) and heated to 60 °C for 1 hour under an argon atmosphere. After cooling the solution to room temperature, the NCM811-Pyr-2D particles were separated using a 200 nm membrane filter (Whatman, UK) and dried overnight in a convection oven at 70 °C. The dried samples were collected and annealed at 300 °C for 2 hours using a tube furnace to enhance the electronic conductivity of Pyr-2D by removing residual functional groups which can inhibit electron transport.

### 3.2.2 Characterization of Materials

The crystal structure was investigated by performing X-ray diffraction (XRD) analysis (SmartLab, Rigaku, Japan) based on Cu K $\alpha$  radiation with  $\lambda = 0.15406$  nm. For the analysis of cycled electrodes, cycled cells were first disassembled under argon atmosphere and the electrodes were washed with ethylene carbonate/diethyl carbonate (EC:DEC=1:1=v/v) followed by vacuum drying overnight. The dried electrode was placed on a glass substrate of an XRD holder (Rigaku, Japan) and the XRD analysis was conducted under ambient atmosphere. The particle morphology was analyzed by aberration-corrected transmission electron microscopy (Cs-TEM, JEM-ARM200F, Japan) and aberration-corrected scanning transmission electron microscopy (Cs-STEM, JEM-ARM200F, Japan). Fourier-

transform infrared (FT-IR, Nicolet 6700, USA) spectra were recorded to characterize the bonding properties of Pyr-2D. The CEI compositions of each cathode were analyzed using XPS (Thermo Scientific Nexsa, USA).

The thermal stability of bare NCM811 and NCM811-Pyr-2D was evaluated by first charging the cells to 4.5 V at the 0.1C rate and then maintained them at 4.5 V for 20 hours. The cells were disassembled under argon atmosphere and washed with ethylene carbonate/diethyl carbonate (EC:DEC=1:1=v/v), followed by drying under vacuum overnight. Samples were prepared for differential scanning calorimetry (DSC)-thermo-gravimetric measurements (DSC 7, Perkin-Elmer, USA) by mixing 3.0 mg of the charged samples with 3  $\mu$ L of electrolyte (1 M LiPF<sub>6</sub> EC:DEC=1:1=v/v) and sealed in an aluminum pan with a hole in the top, before they were scanned at a rate of 10 °C min<sup>-1</sup> from 30 °C to 350 °C. The enthalpy change was obtained by integrating the area of exothermic peak with respect to time.

To evaluate the dissolved amounts of transition metal ions from the bare NCM811 and NCM811-Pyr-2D, each charged cathode was immersed in 2 mL of the electrolyte (1 M LiPF<sub>6</sub> EC:DEC=1:1=v/v) at 60 °C. The sample was taken every week to measure the dissolved amounts of transition metal ions using inductively coupled plasma-atomic emission spectroscopy (ICP-AES, OPTIMA 8300, Perkin-Elmer, USA).

The electric conductivity was measured using the direct current (DC) polarization method. Measurements were conducted by placing powder samples between two stainless steel blocking electrodes. The conductivity ( $\sigma$ ) of each sample was calculated by using the following equation:  $\sigma = t \cdot I / V \cdot A$ , where  $t$  is the thickness of the powder sample,  $I$  is the current,  $V$  is the applied potential, and  $A$  is the area of the contacted electrodes.

### 3.2.3 Electrochemical Evaluation

The NCM cathodes were fabricated by first preparing slurries consisting of a mixture of active material, super P, and poly(vinylidene fluoride) (PVDF) binder with a weight ratio of 8:1:1. The slurries were then cast on Al foil using the doctor blade technique, followed by overnight drying under vacuum at 80 °C. The areal mass loading of the active material was 4.0 mg cm<sup>-2</sup>. The electrochemical performance was characterized by fabricating 2032 coin-type cells. For this, a Li-metal anode with a thickness of 300 nm (Honjo, Japan), a polyethylene separator, and the cathode ( $d=10$  mm) were assembled in an argon-filled glovebox. The electrolyte was 0.2 mL of 1 M LiPF<sub>6</sub> in EC/DEC (1:1 in v/v). The galvanostatic charge-discharge tests were conducted at 25 °C using a battery cycler (WBCS 3000, Won-A Tech, Korea). The cells were cycled in the voltage range of 2.8–4.5 V at 0.1C for the first cycle and at 1C for the subsequent 100 cycles (1C=0.619 mA g<sup>-1</sup>) at 25 and 60 °C. Analysis using electrochemical impedance spectroscopy (EIS) was carried out in the frequency range of 100 kHz to 0.1 Hz using an electrochemical workstation (VSP, Bio-Logic, France). Cyclic voltammetry (CV) was measured under the voltage range of 2.8–4.5 V at the scan rate of 0.1 to 1.0 mV s<sup>-1</sup> using an electrochemical workstation (VSP, Bio-Logic, France).

## 3.3 Results and Discussion

### 3.3.1 Characterization of NCM811-Pyr-2D

A coating of Pyr-2D was applied to the surface of NCM811 by employing the condensation reaction between hexaketocyclohexane and benzenetetramine (Figure 3.1):  $R_1-NH_2 + R_2C=O \rightarrow R_1-N=C-R_2 + H_2O$ . Upon completion of this reaction, Pyr-2D tends to have Vander Waals interaction with NCM811.

Aberration-corrected transmission electron microscopy (Cs-TEM) images of NCM811 particles before and after they were coated with Pyr-2D indicate that the coating layer was uniform with an approximate thickness of 1 nm (Figures 3.2a and b). Energy dispersive X-ray spectroscopy (EDX) mapping with regard to various atoms showed that C and N are uniformly distributed over the surface of the particle, the position of which was detected by mapping Ni, Co, and Mn (Figure 3.2c). This observation reconfirms the uniform distribution of the Pyr-2D coating over the NCM811 particle. Similar distributions of C and N were observed for multiple other NCM811 particles. Thermogravimetric analysis (TGA) indicated the weight portion of Pyr-2D in the NCM811-Pyr-2D sample to be approximately 2 wt% (Figure 3.3). The Fourier-transform infrared (FT-IR) spectrum (Figure 3.2d) exhibited  $-C=N-$  stretching bands at 1465 and 1623  $cm^{-1}$  along with a peak at 877  $cm^{-1}$  originating from the aromatic ring, verifying the existence of the Pyr-2D coating on the NCM811.

X-ray diffraction (XRD) analysis (Figure 3.2e) indicated that the main XRD peaks of both the bare NCM811 and NCM811-Pyr-2D corresponded well with the hexagonal  $\alpha$ - $NaFeO_2$  structure with the  $R\bar{3}m$  space group, implying that the Pyr-2D coating did not alter the original crystal structure of NCM811. A clear splitting of the (006) and (102) peaks verifies<sup>125</sup> that the layered structure was preserved after being coated with the pyrazine-linked 2D sheet. The intensity ratio of  $I(003)/I(104)$  is also known to provide an estimation of the level of TM mixing.<sup>139</sup> In this work,

the intensity ratio decreased from 1.67 to 1.32 after coating with Pyr-2D, indicating increased cation mixing. Scanning transmission electron microscopy (STEM) analysis (Figures 3.2f and g) revealed the appearance of a rock-salt phase with a thickness of  $\sim 3.1$  nm under the  $R\bar{3}m$  space group along the surface of the Pyr-2D-coated NCM811. The formation of these rock-salt phases was verified by the selected area electron diffraction (SAED) pattern of the NCM811-Pyr-2D, which displayed the corresponding diffraction spots. This observation is attributed to the heat treatment during the synthesis of Pyr-2D. In fact, the simple heat treatment of NCM811 at 60 °C in *N*-methyl pyrrolidine (NMP) for 1 hour (denoted as NCM811-preformed-TM) yielded a similar I(003)/I(104) ratio of 1.21 (Figure 3.4). This phenomenon can be understood by considering that, upon heating, the  $\text{Ni}^{3+}$  in NCM811 is reduced to  $\text{Ni}^{2+}$  by NMP,<sup>140</sup> which is liable to cation mixing with  $\text{Li}^+$  on the surface. According to the XPS analysis, the  $\text{Ni}^{3+}$  ions on the surface of NCM811-Pyr-2D were indeed reduced to  $\text{Ni}^{2+}$  (Figure 3.5). These pre-formed divalent Ni ions on the surface construct thin NiO-like rock-salt phase before cycling, which mitigates further significant formation of the same or similar phases during cycling.<sup>141</sup>

The effect of the Pyr-2D coating on the electrical conductivity was assessed by measuring the direct current (DC) polarization of NCM811 before and after the Pyr-2D coating (Figure 3.6). The effect of the thickness of the Pyr-2D coating was determined by additionally preparing a NCM811 sample of which the coating layer of Pyr-2D was five times thicker. The electrical conductivity of bare NCM811 was  $6.46\text{E}-3 \text{ S cm}^{-1}$ , whereas those of NCM811-Pyr-2D ( $\times 1$  and  $\times 5$ ) were  $3.58\text{E}-3 \text{ S cm}^{-1}$  and  $4.85\text{E}-4 \text{ S cm}^{-1}$ , respectively. The decrease in the electrical conductivity of coated NCM811 is ascribed to the lower conductivity of Pyr-2D ( $2.08\text{E}-6 \text{ S cm}^{-1}$ ). Nevertheless, this conductivity is still comparable to those of materials in the NCM family<sup>142</sup> and is far higher than those of widely used coating materials such as  $\text{Al}_2\text{O}_3$  ( $\sim 1.00\text{E}-16 \text{ S cm}^{-1}$ ) and  $\text{LiNbO}_3$  ( $\sim 2.00\text{E}-8 \text{ S cm}^{-1}$ ) (Table 3.1),

although the effect of coating material on electronic conductivity would be limited with limited thickness. Hence, the substantial electrical conductivity and 2D planar morphology for facile coating are the properties on which we mainly focus in the present study of Pyr-2D.

The Li ion diffusion coefficients in the NCM811 and NCM811-Pyr-2D electrodes were retrieved from the cyclic voltammetry (CV) measured at various scan rates from 0.1 to 1.0 mV s<sup>-1</sup> (Figure 3.7) using following equations:

$$i_p = (2.69 \times 10^5) \cdot n^{3/2} \cdot A \cdot D_{Li^+}^{1/2} \cdot C_{Li^+} \cdot v^{1/2} \quad (1)$$

where  $i_p$ ,  $n$ ,  $A$ ,  $D_{Li^+}$ ,  $C_{Li^+}$ , and  $v$  represent peak current (A), number of electron transferred ( $n=1$  for Li<sup>+</sup> ion), cathode area (0.785 cm<sup>2</sup>), Li ion diffusion coefficient (cm<sup>2</sup> s<sup>-1</sup>), Li ion concentration per unit volume (cm<sup>-3</sup>),<sup>128</sup> and scan rate (V s<sup>-1</sup>), respectively. After coating with Pyr-2D, the Li ion diffusion coefficient in the electrode slightly decreased from 2.73×10<sup>-9</sup> to 1.39×10<sup>-9</sup> cm<sup>2</sup> s<sup>-1</sup> for discharging (Table 3.2), implying that the coating layer does not inhibit the Li ion diffusion much in the electrode.

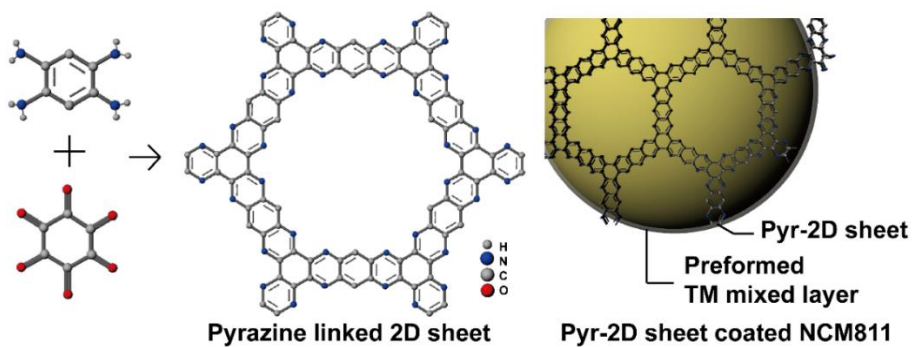


**Figure 3.1** Synthesis scheme of pyrazine-linked 2D sheet (Pyr-2D) and graphical illustration of NCM811 coated with the Pyr-2D sheet (NCM811-Pyr-2D).

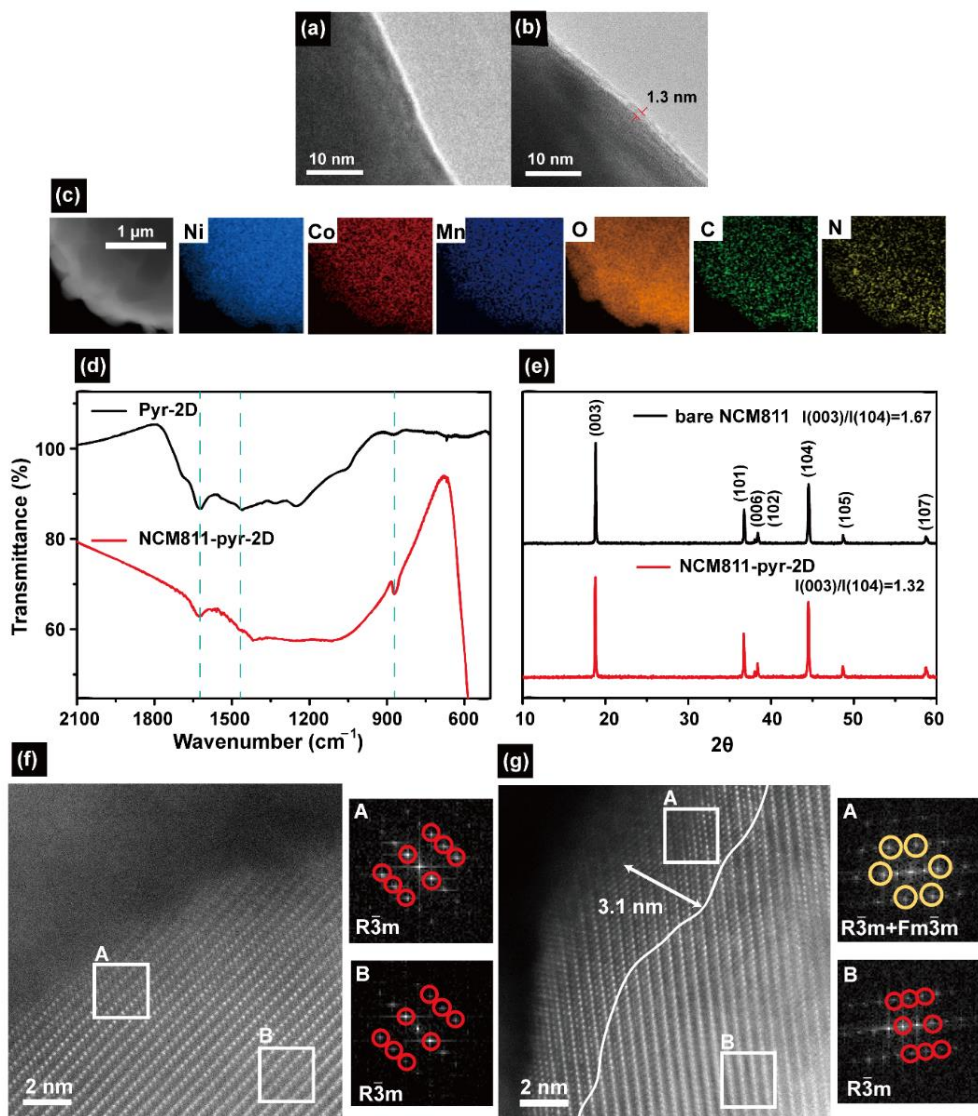


**Figure 3.2** Cs-TEM images of (a) bare NCM811 and (b) NCM811-Pyr-2D. (c) TEM-EDX elemental mapping of NCM811-Pyr-2D with respect to Ni, Co, Mn, C, and N. (d) FT-IR spectra of Pyr-2D and NCM811-Pyr-2D. (e) XRD patterns of bare NCM811 and NCM811-Pyr-2D. Cs-STEM images of (f) bare NCM811 and (g) NCM811-Pyr-2D in the pristine state.

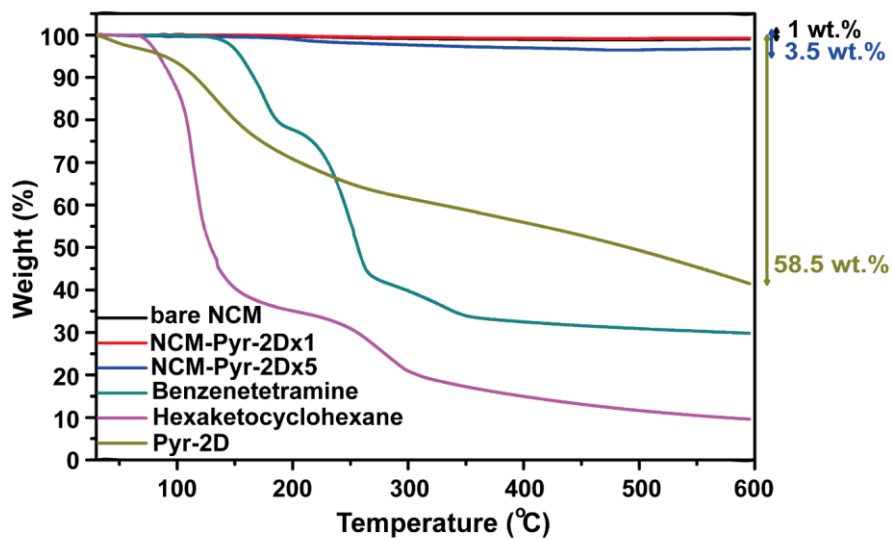


**Figure 3.3** Thermogravimetric analysis (TGA) profiles of bare NCM, NCM-Pyr-2D $\times$ 1, NCM-Pyr-2D $\times$ 5, benzenetetramine, hexaketocyclohexane, and Pyr-2D.

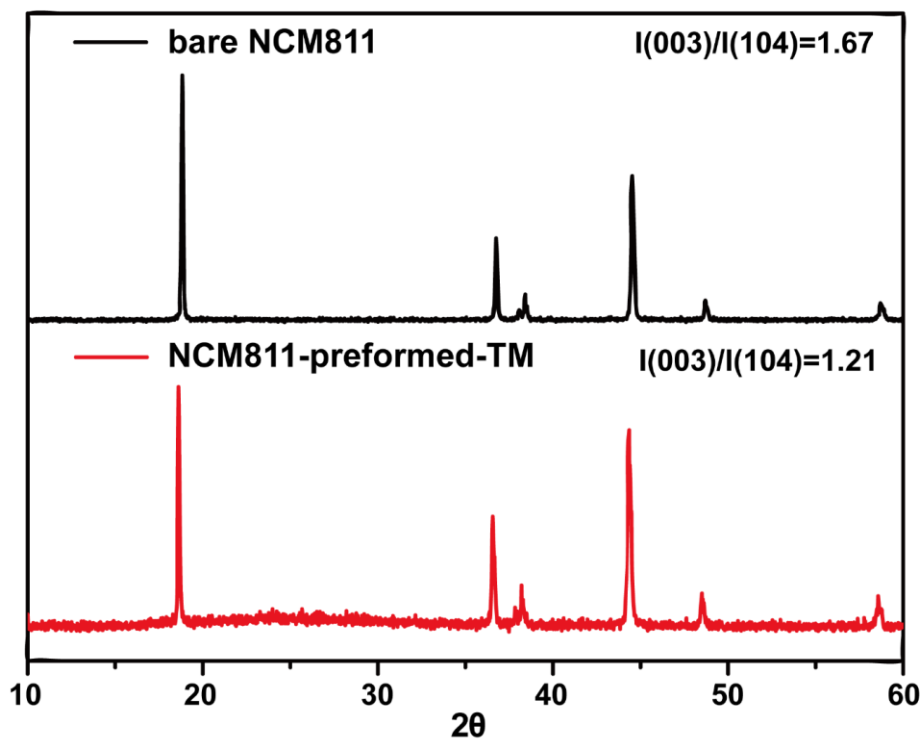


**Figure 3.4** XRD patterns of bare NCM and NCM811-preformed-TM.

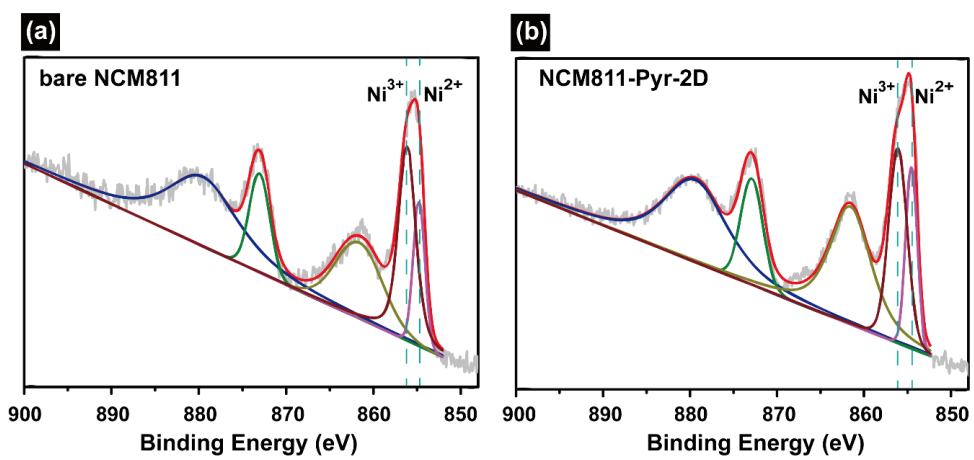


**Figure 3.5** XPS of as-prepared (a) bare NCM811 and (b) NCM811-Pyr-2D in the pristine state.

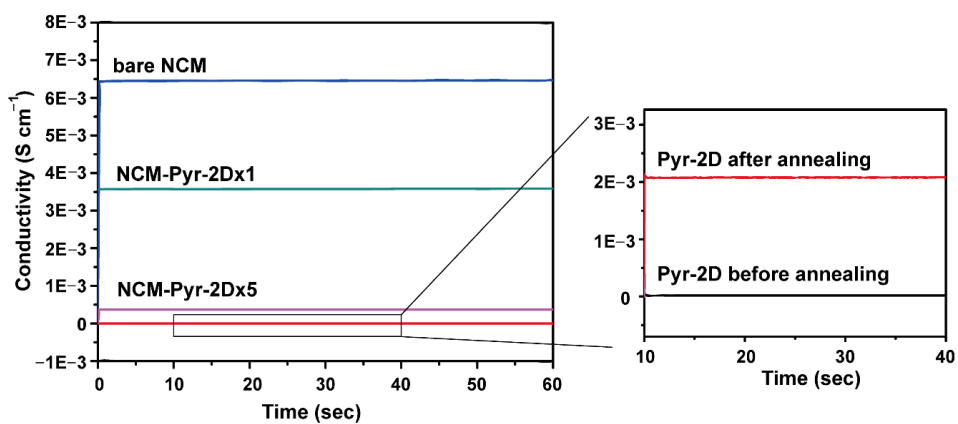


**Figure 3.6** Electronic conductivity of bare NCM, NCM-Pyr-2D $\times$ 1, NCM-Pyr-2D $\times$ 5, and Pyr-2D before and after annealing.

<b>Material</b>	<b>Electric conductivity (S cm<sup>-1</sup>)</b>	<b>Literature information</b>
graphite	2000 (//), 3.3 (a)	
Al <sub>2</sub> O <sub>3</sub>	1.00E-16	
LiNbO <sub>3</sub>	2.00E-8	
Amorphous silicon	3.00E-5	
Iodine doped COF	0.28E-5	<i>Chem. Sci.</i> 2014, 5, 4693
Porphyrine COF	2.38E-6	<i>ACS Appl. Mater. Interfaces</i> 2016, 8, 5366–5375
<b>Pyr-2D before annealing</b>	<b>1.65 E-8</b>	<b>This work</b>
<b>Pyr-2D after annealing</b>	<b>2.08 E-6</b>	<b>This work</b>
<b>bare NCM811</b>	<b>6.46 E-3</b>	<b>This work</b>
<b>NCM-Pyr-2Dx1</b>	<b>3.58 E-3</b>	<b>This work</b>
<b>NCM-Pyr-2Dx5</b>	<b>4.85 E-4</b>	<b>This work</b>

**Table 3.1** Electronic conductivity of representative conductive materials in comparison with those in the current work.

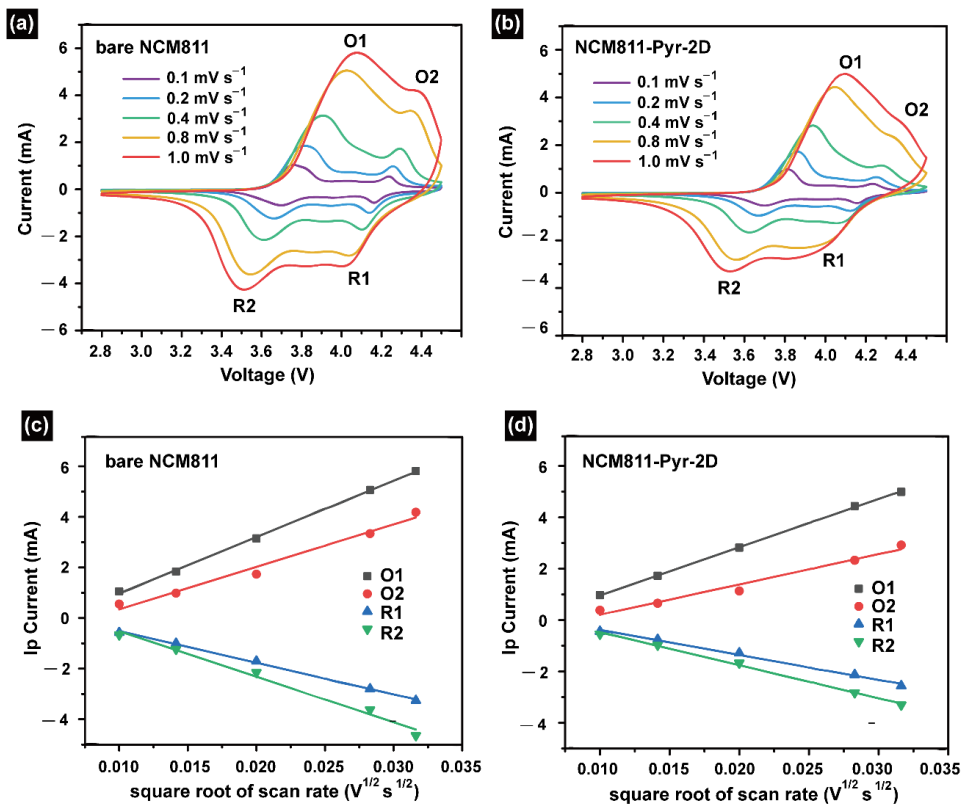


**Figure 3.7** Cyclic-voltammetry of (a) bare NCM811 and (b) NCM811-Pyr-2D. Profiles of peak intensity versus square root of scan rate for (c) bare NCM811 and (d) NCM811-Pyr-2D.

Peak	O1	O2	R1	R2
$D_{Li^+}$ of bare NCM811 ( $\text{cm}^2 \text{s}^{-1}$ )	4.17E-09	2.37E-09	1.32E-09	2.72E-09
$D_{Li^+}$ of NCM811-Pyr-2D ( $\text{cm}^2 \text{s}^{-1}$ )	2.97E-09	1.18E-09	8.02E-10	1.40E-09

**Table 3.2** Lithium ion diffusion coefficients in (a) bare NCM811 and (b) NCM811-Pyr-2D electrodes derived from Figure 3.7.

### 3.3.2 Electrochemical Performance

The electrochemical performance of the bare NCM811 and NCM811-Pyr-2D was evaluated by galvanostatic measurements in the voltage range of 2.8–4.5 V *vs.* Li/Li<sup>+</sup> under Li half-cell configuration. Prior to the battery performance test, cyclic voltammetry (CV) analysis was carried to identify the stable voltage window of Pyr-2D (Figure 3.8). The CV test indicates that Pyr-2D is electrochemically stable in the potential window of 2.8–4.5 V *vs.* Li/Li<sup>+</sup>. The charge-discharge profiles in the 1<sup>st</sup> cycle at 0.1C (Figure 3.9a) reveal that the reversible capacity of the NCM811-Pyr-2D electrode is smaller compared to that of its bare NCM811 counterpart (196.0 *vs.* 210.1 mAh g<sup>-1</sup>) owing to the increased resistance resulting from the addition of Pyr-2D. Also, the NCM811-Pyr-2D electrode exhibited a lower initial Coulombic efficiency (CE): 88.2% *vs.* 90.2%. This observation can be understood in a way that that the Pyr-2D coating induces some reactions more seriously with the electrolyte during the formation of CEI layer in the first charging, leading to a lower initial CE. However, these unwanted parasitic reactions were more serious only in the first cycle, and the CE became higher for NCM811-Pyr-2D than for bare NCM811 in all of the subsequent cycles as a result of the protecting role of the Pyr-2D coating layer against further side reactions. In addition, the NCM811-Pyr-2D electrode exhibited a peak in its very initial discharge stage. This phenomenon is ascribed to its TM mixed surface layer composed of lithium deficient NiO rock-salt phase, which requires extra overpotential for initial Li ion extraction.

In spite of the decreased specific capacity, the NCM811-Pyr-2D electrode achieved more sustainable cyclability compared to that of the bare NCM811 counterpart (Figure 3.9b). When measured at 600.0 mA g<sup>-1</sup> (1C rate) after a formation cycle at 0.1C, the NCM811-Pyr-2D electrode retained 88.8% of its original capacity after 100 cycles, contrary to the 51.2% retention of the bare NCM811 electrode after the same number of cycles. The inferior cyclability of the

bare NCM811 electrode was reflected by its more serious increase in polarization with cycling (Figure 3.10). The NCM811-Pyr-2D also showed higher CEs than those of the bare NCM811 counterpart throughout the cycling range. For example, the CEs of both electrodes were 99.64% vs. 99.42%, respectively, at 100<sup>th</sup> cycle. Apart from this, the NCM811-Pyr-2D exhibited higher rate capability when tested at various C-rates (Figure 3.9c). Although the NCM811-Pyr-2D electrode exhibited slightly lower capacities in the first couple of cycles at 0.1C due to its larger polarizations related to the sacrifice in ionic and electronic conductivity after the Pyr-2D coating, it delivered higher capacities from 0.2C through 2C. For example, at 2C, the NCM811-Pyr-2D electrode achieved 161.2 mAh g<sup>-1</sup> on average, whereas the bare NCM811 electrode showed an average capacity of 102.3 mAh g<sup>-1</sup>. The more significant capacity differences at higher C-rates between both electrodes are attributed to more serious interfacial degradation of the bare NCM811 electrode compared to the NCM811-Pyr-2D electrode that protects its interface with the Pyr-2D coating. The superior cycling and rate performance of the NCM811-Pyr-2D electrode is ascribed to the protective role of the Pyr-2D and its ability to inhibit TM dissolution and side reactions with the electrolyte, both of which are normally accelerated at high voltages.

The effect of the Pyr-2D coating on the cell resistance was investigated by measuring the alternating current (AC) impedance after the 50<sup>th</sup> and 100<sup>th</sup> cycles. As displayed in Figures 3.11a and b, the Nyquist plots of both the bare NCM811 and NCM811-Pyr-2D cells exhibit two semicircles and an incline line in the low-frequency regime. The equivalent circuit is shown in Figure 3.11b in which the resistance of the solution and the Warburg impedance measured in the low-frequency regime are denoted as  $R_s$  and  $W_o$ , respectively. The semicircle in the high-frequency range is known to represent the resistance of the surface film ( $R_f$ ) against Li<sup>+</sup> ion migration. On the other hand, the semicircle in the medium-to-low frequency range is known to indicate the charge transfer resistance ( $R_{ct}$ ) between the electrode and electrolyte. Constant phase elements for film and charge transfer

( $CPE_f$  and  $CPE_{ct}$ ) are non-ideal capacitances from the film and charge transfer, respectively. Although the overall resistance of the NCM811-Pyr-2D was greater than that of the bare NCM811, the increase in resistance of NCM811-Pyr-2D during cycles 50–100 was much smaller. More specifically, the  $R_{ct}$  of bare NCM811 increased by 2.22 times in the cycling range of 50–100, whereas that of NCM811-Pyr-2D increased by only 1.09 times. Based on the fact that the  $R_{ct}$  of NCM811-preformed-TM increased by 1.67 times during cycles 50–100 (Figure 3.12), the changes in the  $R_{ct}$  values of the series of samples point to the critical role of Pyr-2D in protecting the surface. That is, this protective layer mitigates the growth of a resistive layer<sup>58</sup> containing LiF,  $Li_2CO_3$ , and  $Li_xPF_yO_z$  during cycling and also protects against damage resulting from HF attack. Consistent with these EIS results, the XPS analysis in the F 1s branch indicates that peaks corresponding to LiF and  $Li_xPF_yO_z$  were less prominent for NCM811-Pyr-2D after 100 cycles (Figures 3.11 c and d) implying that salt decomposition was less serious in this electrode.

Furthermore, after 100 cycles, the XRD pattern of the NCM811-Pyr-2D electrode showed a far larger I(003)/I(104) ratio of 1.34 compared to that of the bare NCM811 counterpart (1.13) (Figure 3.13a), which suggests lessened cation mixing of the NCM811-Pyr-2D electrode during cycling. Additional confirmation of the beneficial effect of the Pyr-2D layer was obtained by conducting Cs-STEM analysis, which revealed lesser perturbation of the surface structure of the NCM811-Pyr-2D after the 100<sup>th</sup> charge. As shown in Figures 3.13b and c, the thickness of spinel- or rock-salt-like atomic arrangements was smaller near the surface of the NCM811-Pyr-2D compared to the bare NCM811 (3.6 nm vs. 5.1 nm). Once again, these results suggest that the reduced increase in the interfacial resistance and more robust surface structure of NCM811-Pyr-2D originate from the synergistic effect between the protection of the surface by Pyr-2D and the pre-mixed TM atomic arrangement along the surface.

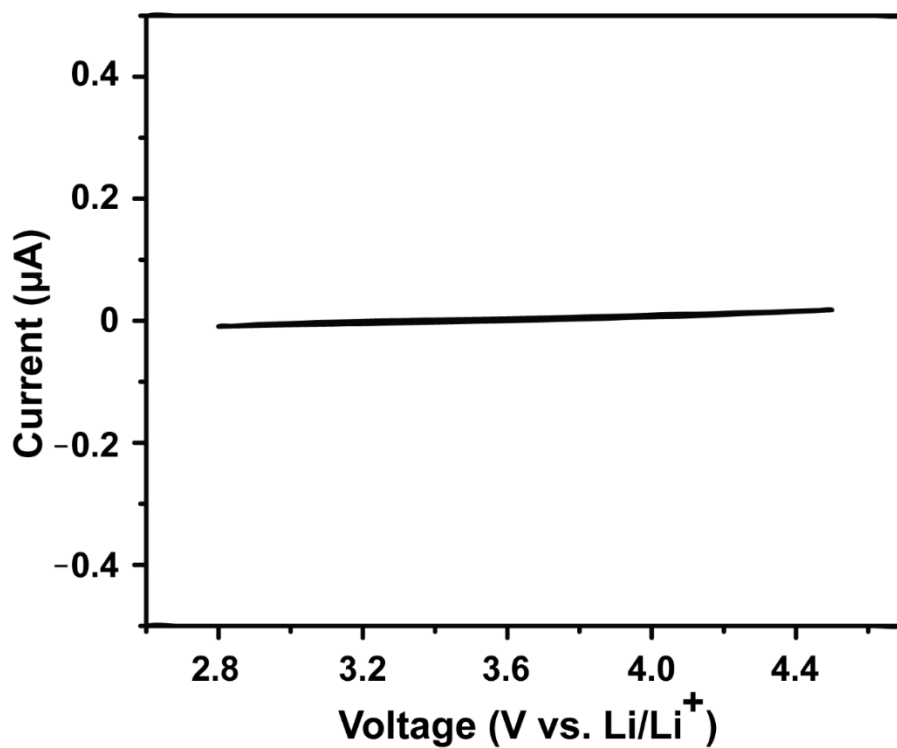


**Figure 3.8** Cyclic voltammetry profile of Pyr-2D at 1C rate.

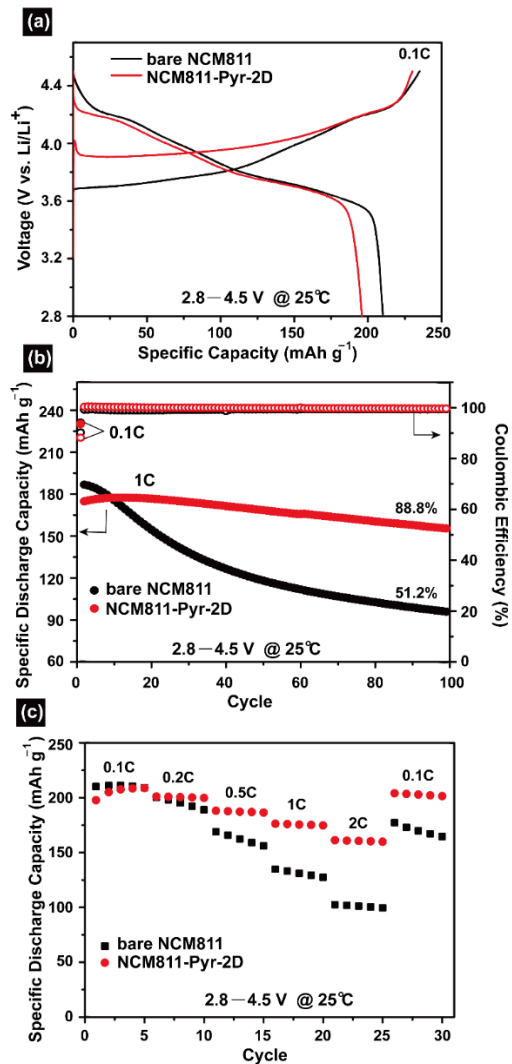


**Figure 3.9** (a) 1<sup>st</sup> charge-discharge profiles at the 0.1C rate. (b) cycling and (c) rate performance of bare NCM811 and NCM811-Pyr-2D.

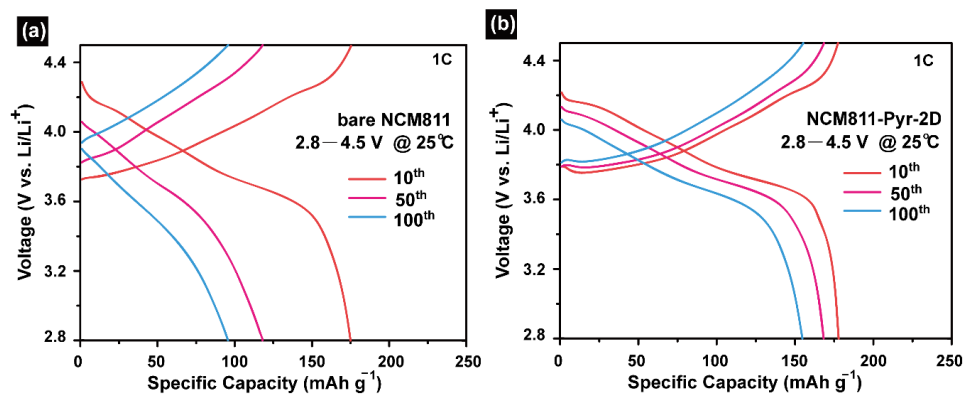


**Figure 3.10** Charge-discharge profiles of (a) bare NCM811 and (b) NCM811-Pyr-2D at different cycle numbers when measured at 1C rate.

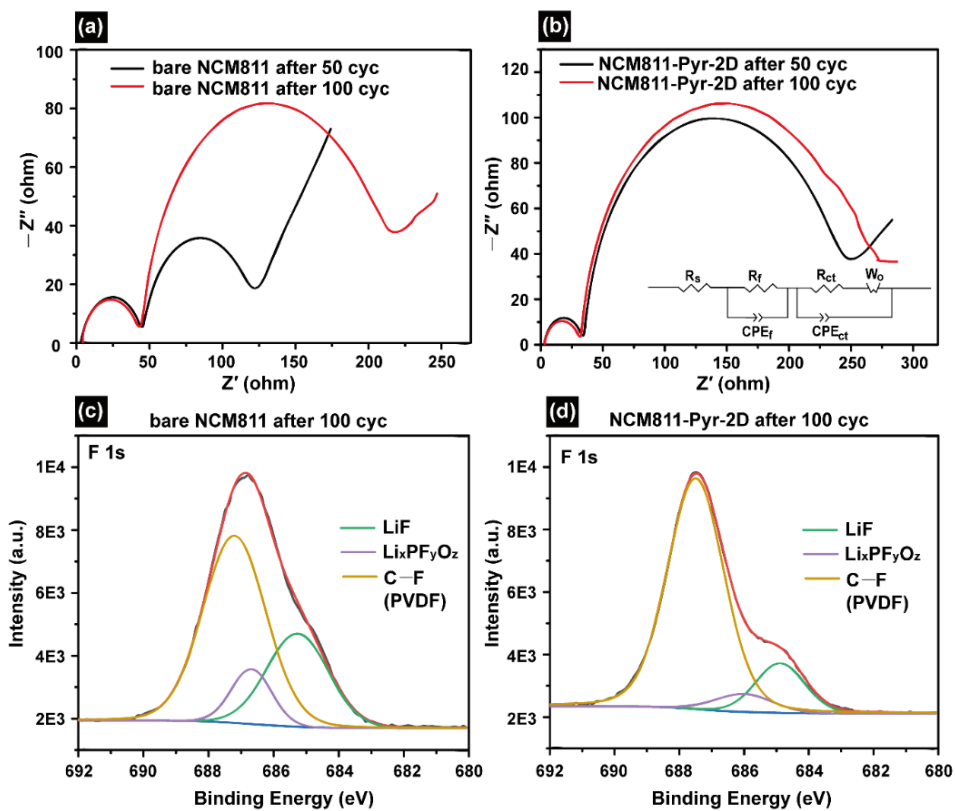


**Figure 3.11** Electrochemical impedance spectroscopy profiles of (a) bare NCM811 and (b) NCM811-Pyr-2D after the 50<sup>th</sup> and 100<sup>th</sup> charge cycles. XPS spectra in the F 1s branch after 100 cycles: (c) bare NCM811 and (d) NCM811-Pyr-2D.

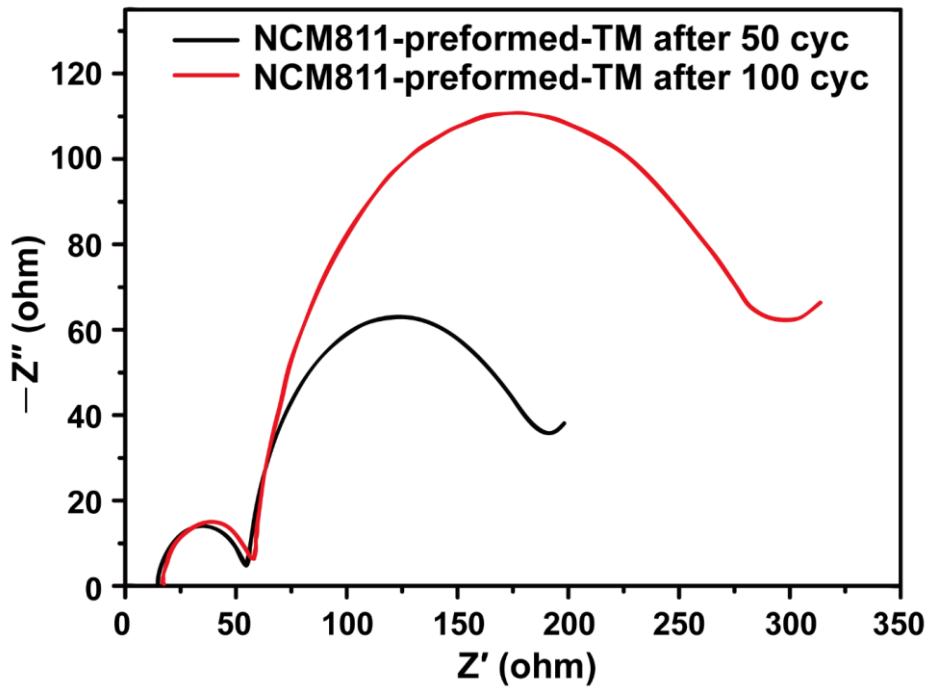


**Figure 3.12** Electrochemical impedance spectroscopy profiles of NCM811-preformed-TM after the 50<sup>th</sup> and 100<sup>th</sup> charge cycle.

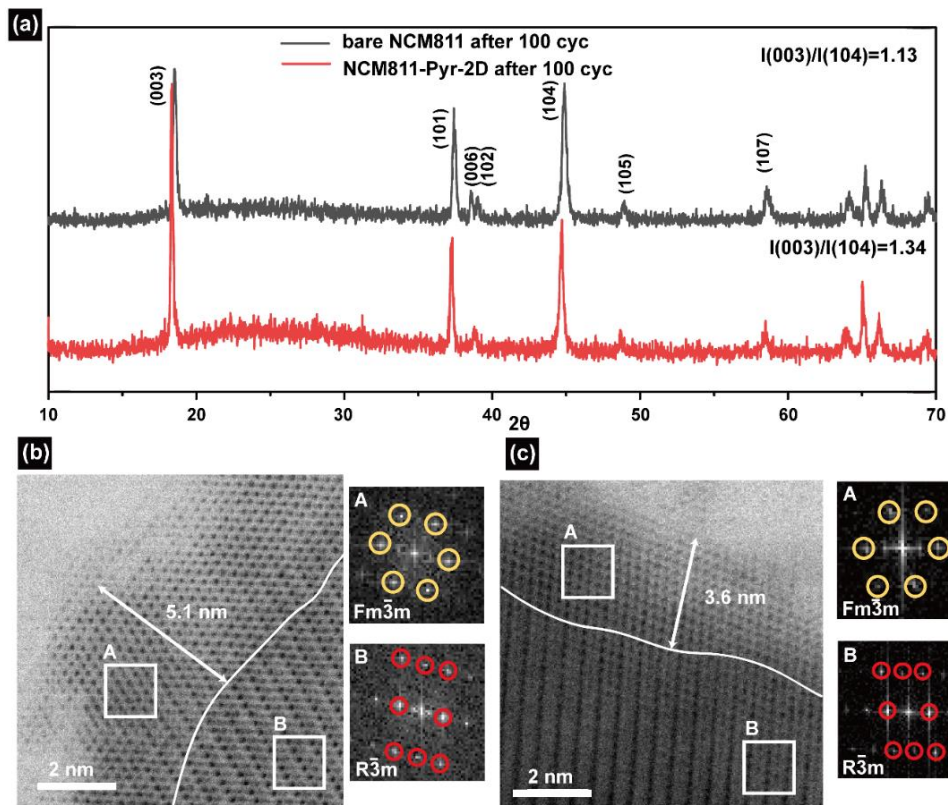


**Figure 3.13** (a) XRD pattern of bare NCM811 and NCM811-Pyr-2D after 100<sup>th</sup> charge. Cs-STEM bright field images of (b) bare NCM811 and (c) NCM811-Pyr-2D after 100<sup>th</sup> charge.

### 3.3.3 Effect of Pyr-2D Coating

The ability of Pyr-2D to protect the surface against the dissolution of TM ions was investigated by measuring the amounts of TM ions that had dissolved at 60 °C after the 1<sup>st</sup> charge. As displayed in Figures 3.14a-c, the amounts of dissolved Ni, Co, and Mn from both the bare NCM811 and NCM811-Pyr-2D electrodes gradually increased with time. TM dissolution is known<sup>128</sup> to mainly occur as a result of attack by HF, which can even be generated from the reaction of trace amounts of water in the electrolyte with LiPF<sub>6</sub>,<sup>127</sup> and is accelerated when cation mixing between TM ions and Li ions occurs at higher temperatures. Among the three TMs, a larger amount of Ni dissolved compared to Co and Mn, presumably owing to the high Ni content of the original composition and its facile exchange with Li.

The thermal stability of charged samples soaked with electrolyte was also examined by differential scanning calorimetry (DSC). According to the DSC profiles in Figure 3.14d, the exothermic peak of the bare NCM811 appears at 223.0 °C, consistent with previous reports,<sup>113, 144</sup> with an enthalpy change of 230.9 J g<sup>-1</sup> whereas the corresponding peak of NCM811-Pyr-2D is located at the higher temperature of 235.6 °C with an enthalpy change of 151.9 J g<sup>-1</sup>. These peaks are associated with the phase transition of NCM811 that involves the release of oxygen species such as O<sub>2</sub><sup>-</sup>, O<sup>-</sup>, O<sub>2</sub><sup>2-</sup>, and O<sub>2</sub>, which can lead to thermal runaway. Thus, the delayed exothermic transition and the smaller enthalpy change revealed by DSC analysis can be interpreted by considering the role of the Pyr-2D in blocking the release of oxygen species, which also contributes to preventing the charged phase from undergoing phase transformation. Indeed, a cycling test at 60 °C proved the enhanced thermal stability of NCM811-Pyr-2D. When measured at 1C, while the bare NCM811 showed 17.9% capacity retention after 100 cycles, NCM811-Pyr-2D retained 68.2% after the same number of cycles (Figure 3.14e).

The cycling performance of the NCM811-Pyr-2D electrode was compared

with that of bare NCM811 with a preformed TM mixed layer (NCM811-preformed-TM) and that of control electrodes coated with the monomers of Pyr-2D (Figure 3.15a), benzenetetramine, and hexaketocyclohexane. These tests were conducted at 1C for 100 cycles at 25 °C, as described above. The NCM811-Pyr-2D electrode retained 88.8% of its original capacity, whereas the bare NCM811, NCM811-preformed-TM, benzenetetramine-coated and hexaketocyclohexane-coated NCM811 electrodes preserved only 51.2, 56.0, 69.2, and 74.6% of their initial capacities, respectively. In addition, the Pyr-2D coating turned out to improve the air stability of NCM811 as indicated by robust cycling performance after different days of air exposure (Figure 3.15b). These results signify that the 2D polymeric network of Pyr-2D is critical for protecting NCM811 particles from undesired side reactions on the surface and crystal damage.

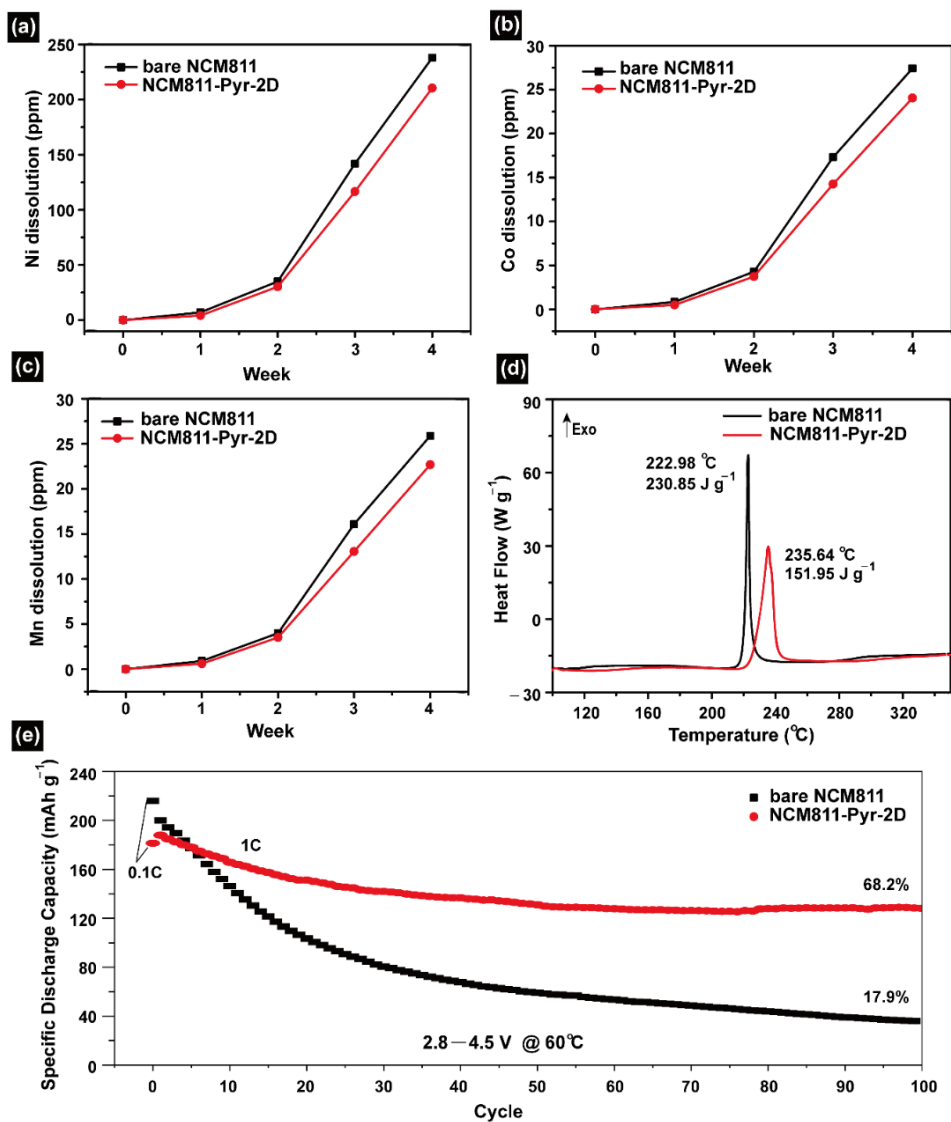


**Figure 3.14** Effect of varied amounts of dissolved (a) Ni, (b) Co, and (c) Mn ions from 1<sup>st</sup> charged NCM811 and NCM811-Pyr-2D at 60  $^{\circ}C$ . (d) DSC profiles of bare NCM811 and NCM811-Pyr-2D with 1 M  $LiPF_6$  EC:DEC(1:1) electrolyte after 1<sup>st</sup> delithiation. (e) Cycling performance of the bare NCM811 and NCM811-Pyr-2D at 60  $^{\circ}C$  when measured at 1C.

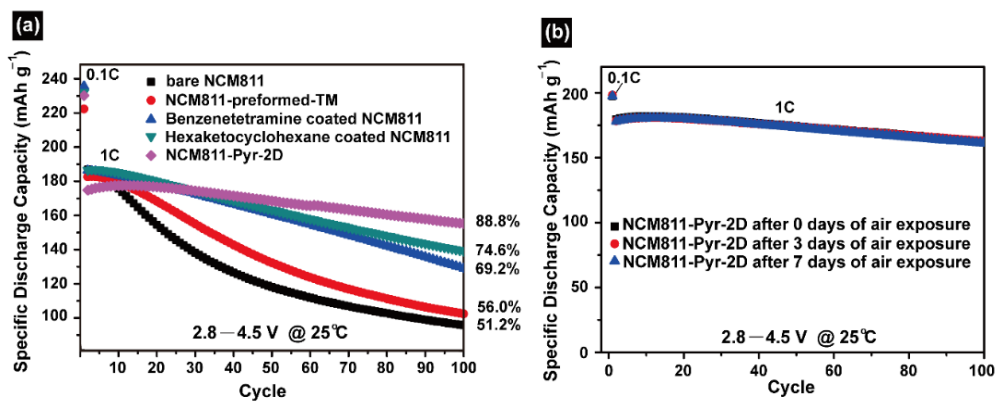


**Figure 3.15** (a) Cycling performance of bare NCM811, NCM811-preformed-TM, benzenetetramine coated NCM811, hexaketocyclohexane coated NCM811 and NCM811-Pyr-2D. (b) Cycling performance of NCM-Pyr-2D with regard to discharging capacity after different days of air exposure.

### 3.4 Conclusion

In an attempt to counteract the performance degradation of Ni-rich NCM811 cathodes, which propagates from the surface of the active particles, we developed a Pyr-2D surface coating. The coating was designed to exploit the 2D planar geometry and conjugated bond configuration of pyrazine. The uniform distribution of the coating and electronic conductivity comparable to that of bare NCM811 served to jointly improve the cycling and rate performance as well as the thermal stability. Additional advantages of the Pyr-2D coating are its ability to largely protect the NCM811 from TM dissolution and unwanted side reactions, apart from the fact that the synthesis of Pyr-2D induces the preformed TM mixed layer that mitigates further TM mixing. Considering that many emerging LIB electrodes are adversely affected by detrimental interfacial instability and an evolution of their surface structure, coating with thinner and electronically conductive 2D covalent organic frameworks is expected to become a key remedy to warrant the electrochemical performance of a wide range of advanced battery electrodes.

## Chapter 4. Summary

In this thesis, the electrolyte/cathode interfaces of Li-O<sub>2</sub> and high Ni NCM batteries were modified with organic molecules. There are two sections: (i) Lewis acidity modified heme catalysts to reduce charging overpotential in Li-O<sub>2</sub> battery, (ii) Pyrazine-linked 2D covalent organic framework coated high-Ni NCM for Li ion battery.

In the first part, the ligand of the heme catalysts was modified with azide and thiocyanate. The electronic charge distribution of the catalysts varied according to the applied ligands. Therefore, the induced Lewis acidity at the Fe active site affected the dissociation of lithium peroxide discharge products. From the density functional theorem calculations, the thiocyanate ligand modified heme catalyst demonstrated the lowest second lithium desorption energy resulting in reduced charging overpotential and elongated cycle life.

In the second part, the pyrazine-linked 2D covalent organic framework was synthesized on the surface of high-Ni NCM cathode materials. The pyrazine-linked covalent organic framework demonstrated not only ionic conductivity through its pore but also electric conductivity. Moreover, together with the preformed TM mixed layer, the Pyr-2D protects the propagation of the TM mixing during cycling. Thus, the cycle life, rate capability as well as the thermal stability enhanced.

## Bibliography

- (1) J.W. Choi, D. Aurbach, Promise and reality of post-lithium-ion batteries with high energy densities, *Nat. Rev. Mater.*, **2016**, 1(4), 16013.
- (2) D. Andre, H. Hain, P. Lamp, F. Maglia, B. Stiaszny, Future high-energy density anode materials from an automotive application perspective, *J. Mater. Chem. A*, **2017**, 5(33), 17174-17198.
- (3) W.B. Luo, X.W. Gao, S.L. Chou, Y.M. Kang, J.Z. Wang, H.K. Liu, S.X. Dou, Investigation of promising air electrode for realizing ultimate lithium oxygen battery, *Adv. Energy Mater.*, **2017**, 7(24), 1700234.
- (4) D. Geng, N. Ding, T.S.A. Hor, S.W. Chien, Z. Liu, D. Wu, X. Sun, Y. Zong, From Lithium-Oxygen to Lithium-Air Batteries: Challenges and Opportunities, *Adv. Energy Mater.*, **2016**, 6(9), 1502164.
- (5) A.C. Luntz, B.D. McCloskey, Nonaqueous Li-air batteries: a status report, *Chem. Rev.*, **2014**, 114(23), 11721-50.
- (6) Y.C. Lu, Z. Xu, H.A. Gasteiger, S. Chen, K. Hamad-Schifferli, Y. Shao-Horn, Platinum–Gold Nanoparticles: A Highly Active Bifunctional Electrocatalyst for Rechargeable Lithium–Air Batteries, *J. Am. Chem. Soc.* **2010**, 132 (35), 12170-12171.
- (7) C.Y. Jung, T.S. Zhao, L. Zeng, P. Tan, Vertically aligned carbon nanotube-ruthenium dioxide core-shell cathode for non-aqueous lithium-oxygen batteries, *J. Power Sources*, **2016**, 331, 82-90.
- (8) H. Gong, H. R. Xue, T. Wang, H. Guo, X. L. Fan, L. Song, W. Xia, J. P. He, High-Loading Nickel Cobaltate Nanoparticles Anchored on Three-Dimensional N-Doped Graphene as an Efficient Bifunctional Catalyst for Lithium–Oxygen Batteries, *ACS Appl. Mater. Interfaces*, **2016**, 8, 18060.
- (9) F. Li, T. Zhang, H. Zhou, Challenges of non-aqueous Li–O<sub>2</sub> batteries: electrolytes, catalysts, and anodes, *Energy Environ. Sci.*, **2013**, 6(4), 1125-

1141.

- (10) V. Etacheri, R. Marom, R. Elazari, G. Salitra, D. Aurbach, Challenges in the development of advanced Li-ion batteries: a review. *Energy Environ. Sci.*, **2011**, *4* (9), 3243-3262.
- (11) J. Liang, L. Wen, X. Yu, F. Li, H.-M. Cheng, Cathode materials: A key challenge for lithium ion batteries. *Energy Storage Mater.*, **2018**, *14*, A1-A3.
- (12) A. Manthiram, J. C. Knight, S.-T. Myung, S.-M. Oh, Y.-K. Sun, Nickel-Rich and Lithium-Rich Layered Oxide Cathodes: Progress and Perspectives. *Adv. Energy Mater.*, **2016**, *6* (1), 1501010.
- (13) S.-T. Myung, F. Maglia, K.-J. Park, C. S. Yoon, P. Lamp, S.-J. Kim, Y.-K. Sun, Nickel-Rich Layered Cathode Materials for Automotive Lithium-Ion Batteries: Achievements and Perspectives. *ACS Energy Lett.*, **2017**, *2* (1), 196-223.
- (14) J. Li, A. Manthiram, A Comprehensive Analysis of the Interphasial and Structural Evolution over Long-Term Cycling of Ultrahigh-Nickel Cathodes in Lithium-Ion Batteries. *Adv. Energy Mater.*, **2019**, 1902731.
- (15) F. Schipper, E. M. Erickson, C. Erk, J.-Y. Shin, F. F. Chesneau, D. Aurbach, Recent advances and remaining challenges for lithium ion battery cathodes I. Nickel-Rich,  $\text{LiNi}_x\text{Co}_y\text{Mn}_z\text{O}_2$ . *J. Electrochem. Soc.*, **2017**, *164* (1), A6220-A6228.
- (16) S. Sharifi-Asl, J. Lu, K. Amine, R. Shahbazian-Yassar, Oxygen Release Degradation in Li-Ion Battery Cathode Materials: Mechanisms and Mitigating Approaches. *Adv. Energy Mater.*, **2019**, *9* (22), 1900551.
- (17) H.-H. Ryu, K.-J. Park, C. S. Yoon, Y.-K. Sun, Capacity Fading of Ni-Rich  $\text{Li}[\text{Ni}_x\text{Co}_y\text{Mn}_{1-x-y}]\text{O}_2$  ( $0.6 \leq x \leq 0.95$ ) Cathodes for High-Energy-Density Lithium-Ion Batteries: Bulk or Surface Degradation? *Chem. Mater.*, **2018**, *30* (3), 1155-1163.
- (18) S. Kalluri, M. Yoon, M. Jo, H. K. Liu, S. X. Dou, J. Cho, Z. Guo,

- Feasibility of Cathode Surface Coating Technology for High-Energy Lithium-ion and Beyond-Lithium-ion Batteries. *Adv. Mater.*, **2017**, *29* (48), 1605807.
- (19) L. David, K. Dahlberg, D. Mohanty, R.E. Ruther, A. Huq, M. Chi, S.J. An, C. Mao, D.M. King, L. Stevenson, D.L. Wood, Unveiling the Role of Al<sub>2</sub>O<sub>3</sub> in Preventing Surface Reconstruction During High-Voltage Cycling of Lithium-Ion Batteries. *ACS Appl. Energy Mater.*, **2019**, *2* (2), 1308-1313.
- (20) U. Woo, C. Yoon, K. Amine, I. Belharouak, Y.-K. Sun, Significant Improvement of Electrochemical Performance of AlF<sub>3</sub>-Coated Li[Ni<sub>0.8</sub>Co<sub>0.1</sub>Mn<sub>0.1</sub>]O<sub>2</sub> Cathode Materials. *J. Electrochem. Soc.* **2007**, *154*, A1005.
- (21) M. Dong, Z. Wang, H. Li, H. Guo, X. Li, K. Shih, J. Wang, Metallurgy Inspired Formation of Homogeneous Al<sub>2</sub>O<sub>3</sub> Coating Layer To Improve the Electrochemical Properties of LiNi<sub>0.8</sub>Co<sub>0.1</sub>Mn<sub>0.1</sub>O<sub>2</sub> Cathode Material. *ACS Sustainable Chem. Eng.* **2017**, *5*, 10199.
- (22) G. Xu, Q. Liu, K.K.S. Lau, Y. Liu, X. Liu, H. Gao, X. Zhou, M. Zhuang, Y. Ren, J. Li, M. Shao, M. Ouyang, F. Pan, Z. Chen, K. Amine, G. Chen, Building ultraconformal protective layers on both secondary and primary particles of layered lithium transition metal oxide cathodes. *Nat. Energy* **2019**, *4*, 484-494.
- (23) F. Wu, J. Liu, L. Li, X. Zhang, R. Luo, Y. Ye, R. Chen, Surface modification of Li-rich cathode materials for lithium-ion batteries with a PEDOT: PSS conducting polymer. *ACS Appl. Mater. Interfaces*, **2016**, *8* (35), 23095-23104.
- (24) Z. Sheng, F. Donald, R. Jeffrey, Discharge characteristic of a non-aqueous electrolyte Li/O<sub>2</sub> battery. *J. Power Sources* **2010**, *195*(4): 1235-1240.
- (25) D. Geng, N. Ding, T.S.A. Hor, S.W. Chien, Z. Liu, D. Wu, X. Sun, Y. Zong, From Lithium-Oxygen to Lithium-Air Batteries: Challenges and

- Opportunities, *Adv. Energy Mater.*, **2016**, 6(9), 1502164.
- (26) W.B. Luo, X.W. Gao, S.L. Chou, Y.M. Kang, J.Z. Wang, H.K. Liu, S.X. Dou, Investigation of promising air electrode for realizing ultimate lithium oxygen battery, *Adv. Energy Mater.*, **2017**, 7(24), 1700234.
- (27) A.C. Luntz, B.D. McCloskey, Nonaqueous Li-air batteries: a status report, *Chem. Rev.*, **2014**, 114(23), 11721-50.
- (28) A. Eftekhari, Energy efficiency: a critically important but neglected factor in battery research, *Sustain. Energ. Fuels*, **2017**, 1(10), 2053-2060.
- (29) J.W. Choi, D. Aurbach, Promise and reality of post-lithium-ion batteries with high energy densities, *Nat. Rev. Mater.*, **2016**, 1(4), 16013.
- (30) D. Andre, H. Hain, P. Lamp, F. Maglia, B. Stiaszny, Future high-energy density anode materials from an automotive application perspective, *J. Mater. Chem. A*, **2017**, 5(33), 17174-17198.
- (31) D. Aurbach, B.D. McCloskey, L.F. Nazar, P.G. Bruce, Advances in understanding mechanisms underpinning lithium-air batteries, *Nat. Energy*, **2016**, 1(9), 1-11.
- (32) F. Li, T. Zhang, H. Zhou, Challenges of non-aqueous Li-O<sub>2</sub> batteries: electrolytes, catalysts, and anodes, *Energy Environ. Sci.*, **2013**, 6(4), 1125-1141.
- (33) H.D. Lim, B. Lee, Y. Bae, H. Park, Y. Ko, H. Kim, J. Kim, K. Kang, Reaction chemistry in rechargeable Li-O<sub>2</sub> batteries, *Chem. Soc. Rev.*, **2017**, 46(10), 2873-2888.
- (34) Z. Peng, S.A. Freunberger, Y. Chen, P.G. Bruce, A reversible and higher-rate Li-O<sub>2</sub> battery, *Science*, **2012**, 1223985.
- (35) L. Johnson, C. Li, Z. Liu, Y. Chen, S.A. Freunberger, P.C. Ashok, B.B. Praveen, K. Dholakia, J.-M. Tarascon, P.G. Bruce, The role of LiO<sub>2</sub> solubility in O<sub>2</sub> reduction in aprotic solvents and its consequences for Li-O<sub>2</sub> batteries, *Nat. Chem.*, **2014**, 6(12), 1091.
- (36) Y.-C. Lu, B.M. Gallant, D.G. Kwabi, J.R. Harding, R.R. Mitchell, M.S.

- Whittingham, Y. Shao-Horn, Lithium-oxygen batteries: bridging mechanistic understanding and battery performance, *Energy Environ. Sci.*, **2013**, 6(3), 750-768.
- (37) B.M. Gallant, R.R. Mitchell, D.G. Kwabi, J. Zhou, L. Zuin, C.V. Thompson, Y. Shao-Horn, Chemical and morphological changes of Li-O<sub>2</sub> battery electrodes upon cycling, *J. Phys. Chem. C*, **2012**, 116(39) 20800-20805.
- (38) Z. Peng, Y. Chen, P. G. Bruce, and Y. Xu, Direct Detection of the Superoxide Anion as a Stable Intermediate in the Electroreduction of Oxygen in a Non-Aqueous Electrolyte Containing Phenol as a Proton Source, *Angew. Chem. Int. Ed.*, **2015**, 54, 8165-8168.
- (39) J. Ren, H. Zhimei, P. K. Kalamate, Y. Shen and Y. Huang, Rotating-disk electrode analysis of the oxidation behavior of dissolved Li<sub>2</sub>O<sub>2</sub> in Li-O<sub>2</sub> batteries, *RSC Adv.*, **2018**, 8, 28496-28502.
- (40) W. Zhang, Y. Shen, D. Sun, Z. Huang, J. Zhou, H. Yan and Y. Huang, Promoting Li<sub>2</sub>O<sub>2</sub> oxidation via solvent-assisted redox shuttle process for low overpotential Li-O<sub>2</sub> battery, *Nano Energy*, **2016**, 30, 43-51.
- (41) B.D. McCloskey, A. Speidel, R. Scheffler, D. Miller, V. Viswanathan, J. Hummelshøj, J. Nørskov, A. Luntz, Twin problems of interfacial carbonate formation in nonaqueous Li-O<sub>2</sub> batteries, *J. Phys. Chem. Lett.*, **2012**, 3(8), 997-1001.
- (42) S. Ganapathy, B.D. Adams, G. Stenou, M.S. Anastasaki, K. Goubitz, X.-F. Miao, L.F. Nazar, M. Wagemaker, Nature of Li<sub>2</sub>O<sub>2</sub> oxidation in a Li-O<sub>2</sub> battery revealed by operando X-ray diffraction, *J. Am. Chem. Soc.*, **2014**, 136(46), 16335-16344.
- (43) B.D. McCloskey, R. Scheffler, A. Speidel, D.S. Bethune, R.M. Shelby, A.C. Luntz, On the efficacy of electrocatalysis in nonaqueous Li-O<sub>2</sub> batteries, *J. Am. Chem. Soc.*, **2011**, 133(45), 18038-18041.
- (44) B.D. McCloskey, A. Valery, A.C. Luntz, S.R. Gowda, G.M. Wallraff, J.M.

- Garcia, T. Mori, L.E. Krupp, Combining accurate O<sub>2</sub> and Li<sub>2</sub>O<sub>2</sub> assays to separate discharge and charge stability limitations in nonaqueous Li–O<sub>2</sub> batteries, *J. Phys. Chem. Lett.*, **2013**, 4(17), 2989-2993.
- (45) V. Viswanathan, J. Nørskov, A. Speidel, R. Scheffler, S. Gowda, A. Luntz, Li–O<sub>2</sub> kinetic overpotentials: Tafel plots from experiment and first-principles theory, *J. Phys. Chem. Lett.*, **2013**, 4(4), 556-560.
- (46) V. Viswanathan, K.S. Thygesen, J. Hummelshøj, J.K. Nørskov, G. Girishkumar, B. McCloskey, A. Luntz, Electrical conductivity in Li<sub>2</sub>O<sub>2</sub> and its role in determining capacity limitations in non-aqueous Li–O<sub>2</sub> batteries, *J. Chem. Phys.*, **2011**, 135(21), 214704.
- (47) A. Débart, A.J. Paterson, J. Bao, P.G. Bruce,  $\alpha$ -MnO<sub>2</sub> Nanowires: A Catalyst for the O<sub>2</sub> Electrode in Rechargeable Lithium Batteries, *Angew. Chem. Int. Ed.*, **2008**, 47(24), 4521-4524.
- (48) Z. Jian, P. Liu, F. Li, P. He, X. Guo, M. Chen, H. Zhou, Core-shell-structured CNT@RuO<sub>2</sub> composite as a high-performance cathode catalyst for rechargeable Li–O<sub>2</sub> batteries, *Angew. Chem. Int. Ed.*, **2014**, 53(2), 442-6.
- (49) F. Li, D.M. Tang, T. Zhang, K. Liao, P. He, D. Golberg, A. Yamada, H. Zhou, Superior Performance of a Li–O<sub>2</sub> Battery with Metallic RuO<sub>2</sub> Hollow Spheres as the Carbon-Free Cathode, *Adv. Energy Mater.*, **2015**, 5(13), 1500294.
- (50) S. Ma, L. Sun, L. Cong, X. Gao, C. Yao, X. Guo, L. Tai, P. Mei, Y. Zeng, H. Xie, Multiporous MnCo<sub>2</sub>O<sub>4</sub> microspheres as an efficient bifunctional catalyst for nonaqueous Li–O<sub>2</sub> batteries, *J. Phys. Chem. C*, **2013**, 117(49), 25890-25897.
- (51) S.H. Oh, L.F. Nazar, Oxide Catalysts for Rechargeable High-Capacity Li–O<sub>2</sub> Batteries, *Adv. Energy Mater.*, **2012**, 2(7), 903-910.
- (52) H.W. Park, D.U. Lee, L.F. Nazar, Z. Chen, Oxygen reduction reaction using MnO<sub>2</sub> nanotubes/nitrogen-doped exfoliated graphene hybrid catalyst

- for Li–O<sub>2</sub> battery applications, *J. Electrochem. Soc.*, **2013**, *160*(2), A344–A350.
- (53) W.H. Ryu, T.H. Yoon, S.H. Song, S. Jeon, Y.J. Park, I.D. Kim, Bifunctional composite catalysts using Co<sub>3</sub>O<sub>4</sub> nanofibers immobilized on nonoxidized graphene nanoflakes for high-capacity and long-cycle Li–O<sub>2</sub> batteries, *Nano. Lett.*, **2013**, *13*(9), 4190–7.
- (54) H. Wang, Y. Yang, Y. Liang, G. Zheng, Y. Li, Y. Cui, H. Dai, Rechargeable Li–O<sub>2</sub> batteries with a covalently coupled MnCo<sub>2</sub>O<sub>4</sub>–graphene hybrid as an oxygen cathode catalyst, *Energy Environ. Sci.*, **2012**, *5*(7), 7931–7935.
- (55) E. Yilmaz, C. Yogi, K. Yamanaka, T. Ohta, H.R. Byon, Promoting formation of noncrystalline Li<sub>2</sub>O<sub>2</sub> in the Li–O<sub>2</sub> battery with RuO<sub>2</sub> nanoparticles, *Nano. Lett.*, **2013**, *13*(10), 4679–84.
- (56) Y. Lei, J. Lu, X. Luo, T. Wu, P. Du, X. Zhang, Y. Ren, J. Wen, D.J. Miller, J.T. Miller, Synthesis of porous carbon supported palladium nanoparticle catalysts by atomic layer deposition: application for rechargeable lithium–O<sub>2</sub> battery, *Nano. Lett.*, **2013**, *13*(9), 4182–4189.
- (57) F. Li, D.M. Tang, Y. Chen, D. Golberg, H. Kitaura, T. Zhang, A. Yamada, H. Zhou, Ru/ITO: a carbon-free cathode for nonaqueous Li–O<sub>2</sub> battery, *Nano. Lett.*, **2013**, *13*(10), 4702–4707.
- (58) Y.-C. Lu, Z. Xu, H.A. Gasteiger, S. Chen, K. Hamad-Schifferli, Y. Shao-Horn, Platinum–gold nanoparticles: a highly active bifunctional electrocatalyst for rechargeable lithium-air batteries, *J. Am. Chem. Soc.*, **2010**, *132*(35), 12170–12171.
- (59) B.D. McCloskey, R. Scheffler, A. Speidel, D.S. Bethune, R.M. Shelby, A.C. Luntz, On the efficacy of electrocatalysis in nonaqueous Li–O<sub>2</sub> batteries, *J. Am. Chem. Soc.*, **2011**, *133*(45), 18038–41.
- (60) J. Zhu, X. Ren, J. Liu, W. Zhang, Z. Wen, Unraveling the Catalytic Mechanism of Co<sub>3</sub>O<sub>4</sub> for the Oxygen Evolution Reaction in a Li–O<sub>2</sub>

- Battery, *ACS Catal.*, **2014**, *5*(1), 73-81.
- (61) B.G. Kim, H.J. Kim, S. Back, K.W. Nam, Y. Jung, Y.K. Han, J.W. Choi, Improved reversibility in lithium-oxygen battery: understanding elementary reactions and surface charge engineering of metal alloy catalyst, *Sci. Rep.*, **2014**, *4*, 4225.
- (62) H.-J. Kim, S.C. Jung, Y.-K. Han, S.H. Oh, An atomic-level strategy for the design of a low overpotential catalyst for Li–O<sub>2</sub> batteries, *Nano Energy*, **2015**, *13*, 679-686.
- (63) Z. Lyu, L. Yang, Y. Luan, X. Renshaw Wang, L. Wang, Z. Hu, J. Lu, S. Xiao, F. Zhang, X. Wang, F. Huo, W. Huang, Z. Hu, W. Chen, Effect of oxygen adsorbability on the control of Li<sub>2</sub>O<sub>2</sub> growth in Li–O<sub>2</sub> batteries: Implications for cathode catalyst design, *Nano Energy*, **2017**, *36*, 68-75.
- (64) L. Shi, A. Xu, T. Zhao, RuO<sub>2</sub> Monolayer: A Promising Bifunctional Catalytic Material for Nonaqueous Lithium-Oxygen Batteries, *J. Phys. Chem. C*, **2016**, *120*(12), 6356-6362.
- (65) L. Shi, T. Zhao, A. Xu, Z. Wei, Unraveling the Catalytic Mechanism of Rutile RuO<sub>2</sub> for the Oxygen Reduction Reaction and Oxygen Evolution Reaction in Li–O<sub>2</sub> Batteries, *ACS Catal.*, **2016**, *6*(9), 6285-6293.
- (66) J. Zhu, F. Wang, B. Wang, Y. Wang, J. Liu, W. Zhang, Z. Wen, Surface Acidity as Descriptor of Catalytic Activity for Oxygen Evolution Reaction in Li–O<sub>2</sub> Battery, *J. Am. Chem. Soc.*, **2015**, *137*(42), 13572-9.
- (67) T.P. Khaket, R. Ahmad, Biochemical studies on hemoglobin modified with reactive oxygen species (ROS), *Appl. Biochem. Biotechnol.*, **2011**, *164*(8), 1422-30.
- (68) T. Yamashita, L. Hafsi, E. Masuda, H. Tsujino, T. Uno, Ferric human neuroglobin scavenges superoxide to form oxy adduct, *Chem. Pharm. Bull.*, **2014**, *62*(6), 613-615.
- (69) W.H. Ryu, F.S. Gittleson, J.M. Thomsen, J. Li, M.J. Schwab, G.W. Brudvig, A.D. Taylor, Heme biomolecule as redox mediator and oxygen

- shuttle for efficient charging of lithium-oxygen batteries, *Nat. Commun.*, **2016**, *7*, 12925.
- (70) R.T. Tom, T. Pradeep, Interaction of azide ion with hemin and cytochrome c immobilized on Au and Ag nanoparticles, *Langmuir*, **2005**, *21*(25), 11896-11902.
- (71) C.-J. Gu, F.-Y. Kong, Z.-D. Chen, D.-H. Fan, H.-L. Fang, W. Wang, Bioelectronics, Reduced graphene oxide-Hemin-Au nanohybrids: Facile one-pot synthesis and enhanced electrocatalytic activity towards the reduction of hydrogen peroxide, *Biosensors*, **2016**, *78*, 300-307.
- (72) T. Zhang, L. Wang, C. Gao, C. Zhao, Y. Wang, J. Wang, Hemin immobilized into metal-organic frameworks as an electrochemical biosensor for 2,4,6-trichlorophenol, *Nanotechnology*, **2018**, *29*(7), 074003.
- (73) B.G. Kim, S. Kim, H. Lee, J.W. Choi, Wisdom from the Human Eye: A Synthetic Melanin Radical Scavenger for Improved Cycle Life of Li-O<sub>2</sub> Battery, *Chem. Mater.*, **2014**, *26*(16), 4757-4764.
- (74) C. Wu, T. Li, C. Liao, L. Li, J. Yang, Tea polyphenol-inspired tannic acid-treated polypropylene membrane as a stable separator for lithium-oxygen batteries, *J. Mater. Chem. A*, **2017**, *5*(25), 12782-12786.
- (75) Y. Liu, L. Wang, L. Cao, C. Shang, Z. Wang, H. Wang, L. He, J. Yang, H. Cheng, J. Li, Understanding and suppressing side reactions in Li-air batteries, *Mater. Chem. Front.*, **2017**, *1*(12), 2495-2510.
- (76) M.D. Radin, C.W. Monroe, D.J. Siegel, Impact of Space-Charge Layers on Sudden Death in Li/O<sub>2</sub> Batteries, *J. Phys. Chem. Lett.*, **2015**, *6*(15), 3017-22.
- (77) D. Enslin, M. Stjerndahl, A. Nyttén, T. Gustafsson, J. Thomas, A comparative XPS surface study of Li<sub>2</sub>FeSiO<sub>4</sub>/C cycled with LiTFSI-and LiPF<sub>6</sub>-based electrolytes, *J. Mater. Chem.*, **2009**, *19*(1), 82-88.
- (78) D.J. Lee, H. Lee, J. Song, M.-H. Ryou, Y.M. Lee, H.-T. Kim, J.-K. Park, Composite protective layer for Li metal anode in high-performance

- lithium-oxygen batteries, *Electrochem. Commun.*, **2014**, *40*, 45-48.
- (79) K. Burger, H. Ebel, XPS (ESCA) characterization of spin-state crossover in an iron(II) mixed complex, *Inorg. Chim. Acta*, **1981**, *53*, L105-L107.
- (80) Q. Tu, L. Zhao, X. Han, D.-E. Wang, M.-S. Yuan, C. Tian, J. Wang, A visualized method for Cu<sup>2+</sup> ion detection by self-assembling azide functionalized free graphene oxide using click chemistry, *RSC Adv.*, **2016**, *6*(98), 95628-95632.
- (81) W. Zhu, W. Li, C. Wang, J. Cui, H. Yang, Y. Jiang, G. Li, CB [8]-based rotaxane as a useful platform for sensitive detection and discrimination of explosives, *Chem. Sci.*, **2013**, *4*(9), 3583-3590.
- (82) B. Hammer, J.K. Nørskov, Theoretical surface science and catalysis-calculations and concepts, *Advances in catalysis*, Elsevier2000, pp. 71-129.
- (83) A. Nilsson, L.G. Pettersson, J. Norskov, Chemical bonding at surfaces and interfaces, Elsevier2011.
- (84) V. Stamenkovic, B.S. Mun, K.J. Mayrhofer, P.N. Ross, N.M. Markovic, J. Rossmeisl, J. Greeley, J.K. Nørskov, Changing the activity of electrocatalysts for oxygen reduction by tuning the surface electronic structure, *Angew. Chem. Int. Ed.*, **2006**, *118*(18), 2963-2967.
- (85) J. Sun, Y.-H. Fang, Z.-P. Liu, Electrocatalytic oxygen reduction kinetics on Fe-center of nitrogen-doped graphene, *Phys. Chem. Chem. Phys.*, **2014**, *16*(27), 13733-13740.
- (86) J. W. Choi, D. Aurbach, Promise and reality of post-lithium-ion batteries with high energy densities. *Nat. Rev. Mater.*, **2016**, *1* (4), 16013.
- (87) V. Etacheri, R. Marom, R. Elazari, G. Salitra, D. Aurbach, Challenges in the development of advanced Li-ion batteries: a review. *Energy Environ. Sci.*, **2011**, *4* (9), 3243-3262.
- (88) A. Manthiram, B. Song, W. Li, A perspective on nickel-rich layered oxide cathodes for lithium-ion batteries. *Energy Storage Mater.*, **2017**, *6*, 125-

139.

- (89) A. Manthiram, J.C. Knight, S.-T. Myung, S.-M. Oh, Y.-K. Sun, Nickel-Rich and Lithium-Rich Layered Oxide Cathodes: Progress and Perspectives. *Adv. Energy Mater.*, **2016**, 6 (1), 1501010.
- (90) J. Li, A. Manthiram, A Comprehensive Analysis of the Interphasial and Structural Evolution over Long-Term Cycling of Ultrahigh-Nickel Cathodes in Lithium-Ion Batteries. *Adv. Energy Mater.*, **2019**, 1902731.
- (91) S.-T. Myung, F. Maglia, K.-J. Park, C.S. Yoon, P. Lamp, S.-J. Kim, Y.-K. Sun, Nickel-Rich Layered Cathode Materials for Automotive Lithium-Ion Batteries: Achievements and Perspectives. *ACS Energy Lett.*, **2017**, 2 (1), 196-223.
- (92) J. Xu, F. Lin, M.M. Doeff, W. Tong, A review of Ni-based layered oxides for rechargeable Li-ion batteries. *J. Mater. Chem. A*, **2017**, 5 (3), 874-901.
- (93) W. Liu, P. Oh, X. Liu, M.J. Lee, W. Cho, S. Chae, Y. Kim, J. Cho, Nickel-rich layered lithium transition-metal oxide for high-energy lithium-ion batteries. *Angew. Chem. Int. Ed.*, **2015**, 54 (15), 4440-4457.
- (94) F. Schipper, E.M. Erickson, C. Erk, J.-Y. Shin, F.F. Chesneau, D. Aurbach, Recent advances and remaining challenges for lithium ion battery cathodes I. Nickel-Rich,  $\text{LiNi}_x\text{Co}_y\text{Mn}_z\text{O}_2$ . *J. Electrochem. Soc.*, **2017**, 164 (1), A6220-A6228.
- (95) J. Liang, L. Wen, X. Yu, F. Li, H.-M. Cheng, Cathode materials: A key challenge for lithium ion batteries. *Energy Storage Mater.*, **2018**, 14, A1-A3.
- (96) S.S. Zhang, Problems and their origins of Ni-rich layered oxide cathode materials. *Energy Storage Mater.*, **2019**.
- (97) S. Sharifi-Asl, J. Lu, K. Amine, R. Shahbazian-Yassar, Oxygen Release Degradation in Li-Ion Battery Cathode Materials: Mechanisms and Mitigating Approaches. *Adv. Energy Mater.*, **2019**, 9 (22), 1900551.
- (98) H.-H. Ryu, K.-J. Park, C.S. Yoon, Y.-K. Sun, Capacity Fading of Ni-Rich

- Li[Ni<sub>x</sub>Co<sub>y</sub>Mn<sub>1-x-y</sub>]O<sub>2</sub> (0.6 ≤ x ≤ 0.95) Cathodes for High-Energy-Density Lithium-Ion Batteries: Bulk or Surface Degradation? *Chem. Mater.*, **2018**, *30* (3), 1155-1163.
- (99) M. Dixit, B. Markovsky, F. Schipper, D. Aurbach, D.T. Major, Origin of Structural Degradation During Cycling and Low Thermal Stability of Ni-Rich Layered Transition Metal-Based Electrode Materials. *J. Phys. Chem. C*, **2017**, *121* (41), 22628-22636.
- (100) S.-K. Jung, H. Gwon, J. Hong, K.-Y. Park, D.-H. Seo, H. Kim, J. Hyun, W. Yang, K. Kang, Understanding the Degradation Mechanisms of LiNi<sub>0.5</sub>Co<sub>0.2</sub>Mn<sub>0.3</sub>O<sub>2</sub> Cathode Material in Lithium Ion Batteries. *Adv. Energy Mater.*, **2014**, *4* (1), 1300787.
- (101) C. Liang, F. Kong, R.C. Longo, S. Kc, J.-S. Kim, S. Jeon, S. Choi, K. Cho, Unraveling the Origin of Instability in Ni-Rich LiNi<sub>1-2x</sub>Co<sub>x</sub>Mn<sub>x</sub>O<sub>2</sub> (NCM) Cathode Materials. *J. Phys. Chem. C*, **2016**, *120* (12), 6383-6393.
- (102) F. Schipper, M. Dixit, D. Kovacheva, M. Talianker, O. Haik, J. Grinblat, E.M. Erickson, C. Ghanty, D.T. Major, B. Markovsky, D. Aurbach, Stabilizing nickel-rich layered cathode materials by a high-charge cation doping strategy: zirconium-doped LiNi<sub>0.6</sub>Co<sub>0.2</sub>Mn<sub>0.2</sub>O<sub>2</sub>. *J. Mater. Chem. A*, **2016**, *4* (41), 16073-16084.
- (103) J. Yang, Y. Xia, Enhancement on the cycling stability of the layered Ni-rich oxide cathode by in-situ fabricating nano-thickness cation-mixing layers. *J. Electrochem. Soc.*, **2016**, *163* (13), A2665-A2672.
- (104) T. Yim, K.S. Kang, J. Mun, S.H. Lim, S.-G. Woo, K.J. Kim, M.-S. Park, W. Cho, J.H. Song, Y.-K. Han, J.-S. Yu, Y.-J. Kim, Understanding the effects of a multi-functionalized additive on the cathode–electrolyte interfacial stability of Ni-rich materials. *J. Power Sources*, **2016**, *302*, 431-438.
- (105) S.-W. Lee, M.-S. Kim, J. H. Jeong, D.-H. Kim, K.Y. Chung, K.C. Roh, K.-B. Kim, Li<sub>3</sub>PO<sub>4</sub> surface coating on Ni-rich LiNi<sub>0.6</sub>Co<sub>0.2</sub>Mn<sub>0.2</sub>O<sub>2</sub> by a citric

- acid assisted sol-gel method: Improved thermal stability and high-voltage performance. *J. Power Sources*, **2017**, *360*, 206-214.
- (106) A.O. Kondrakov, A. Schmidt, J. Xu, H. Geßwein, R. Mönig, P. Hartmann, H. Sommer, T. Brezesinski, J. Janek, Anisotropic Lattice Strain and Mechanical Degradation of High- and Low-Nickel NCM Cathode Materials for Li-Ion Batteries. *J. Phys. Chem. C*, **2017**, *121* (6), 3286-3294.
- (107) L. de Biasi, B. Schwarz, T. Brezesinski, P. Hartmann, J. Janek, H. Ehrenberg, Chemical, Structural, and Electronic Aspects of Formation and Degradation Behavior on Different Length Scales of Ni-Rich NCM and Li-Rich HE-NCM Cathode Materials in Li-Ion Batteries. *Adv. Mater.*, **2019**, *31* (26), 1900985.
- (108) J.-M. Lim, T. Hwang, D. Kim, M.-S. Park, K. Cho, M. Cho, Intrinsic Origins of Crack Generation in Ni-rich  $\text{LiNi}_{0.8}\text{Co}_{0.1}\text{Mn}_{0.1}\text{O}_2$  Layered Oxide Cathode Material. *Sci. Rep.*, **2017**, *7*, 39669.
- (109) P. Yan, J. Zheng, M. Gu, J. Xiao, J.-G. Zhang, C.-M. Wang, Intragranular cracking as a critical barrier for high-voltage usage of layer-structured cathode for lithium-ion batteries. *Nat. Commun.*, **2017**, *8* (1), 14101.
- (110) H.-H. Sun, A. Manthiram, Impact of Microcrack Generation and Surface Degradation on a Nickel-Rich Layered  $\text{Li}[\text{Ni}_{0.9}\text{Co}_{0.05}\text{Mn}_{0.05}]\text{O}_2$  Cathode for Lithium-Ion Batteries. *Chem. Mater.*, **2017**, *29* (19), 8486-8493.
- (111) S. Kalluri, M. Yoon, M. Jo, H.K. Liu, S.X. Dou, J. Cho, Z. Guo, Feasibility of Cathode Surface Coating Technology for High-Energy Lithium-ion and Beyond-Lithium-ion Batteries. *Adv. Mater.*, **2017**, *29* (48), 1605807.
- (112) Z. Chen, Y. Qin, K. Amine, Y.K. Sun, Role of surface coating on cathode materials for lithium-ion batteries. *J. Mater. Chem.*, **2010**, *20* (36), 7606-7612.
- (113) G.-L. Xu, Q. Liu, K.K. Lau, Y. Liu, X. Liu, H. Gao, X. Zhou, M. Zhuang, Y. Ren, J. Li, Building ultraconformal protective layers on both secondary and primary particles of layered lithium transition metal oxide cathodes.

- Nat. Energy*, **2019**, 4, 484-494.
- (114) P. Guan, L. Zhou, Z. Yu, Y. Sun, Y. Liu, F. Wu, Y. Jiang, D. Chu, Recent progress of surface coating on cathode materials for high-performance lithium-ion batteries. *J. Energy Chem.*, **2020**, 43, 220-235.
- (115) L. David, K. Dahlberg, D. Mohanty, R.E. Ruther, A. Huq, M. Chi, S.J. An, C. Mao, D.M. King, L. Stevenson, D.L. Wood, Unveiling the Role of Al<sub>2</sub>O<sub>3</sub> in Preventing Surface Reconstruction During High-Voltage Cycling of Lithium-Ion Batteries. *ACS Appl. Energy Mater.*, **2019**, 2 (2), 1308-1313.
- (116) Y. Shi, M. Zhang, D. Qian, Y. S. Meng, Ultrathin Al<sub>2</sub>O<sub>3</sub> coatings for improved cycling performance and thermal stability of LiNi<sub>0.5</sub>Co<sub>0.2</sub>Mn<sub>0.3</sub>O<sub>2</sub> cathode material. *Electrochim. Acta*, **2016**, 203, 154-161.
- (117) J. Guo, Y. Xu, S. Jin, L. Chen, T. Kaji, Y. Honsho, M. Addicoat, J. Kim, A. Saeki, H. Ihee, S. Seki, S. Irle, M. Hiramoto, J. Gao, D. Jiang, Conjugated organic framework with three-dimensionally ordered stable structure and delocalized  $\pi$  clouds. *Nat. Commun.*, **2013**, 4, 2736.
- (118) X. Li, L. Jin, D. Song, H. Zhang, X. Shi, Z. Wang, L. Zhang, L. Zhu, LiNbO<sub>3</sub>-coated LiNi<sub>0.8</sub>Co<sub>0.1</sub>Mn<sub>0.1</sub>O<sub>2</sub> cathode with high discharge capacity and rate performance for all-solid-state lithium battery. *J. Energy Chem.*, **2020**, 40, 39-45.
- (119) W. Cho, S.-M. Kim, J.H. Song, T. Yim, S.-G. Woo, K.-W. Lee, J.-S. Kim, Y.-J. Kim, Improved electrochemical and thermal properties of nickel rich LiNi<sub>0.6</sub>Co<sub>0.2</sub>Mn<sub>0.2</sub>O<sub>2</sub> cathode materials by SiO<sub>2</sub> coating. *J. Power Sources*, **2015**, 282, 45-50.
- (120) F. Schipper, H. Bouzaglo, M. Dixit, E.M. Erickson, T. Weigel, M. Talianker, J. Grinblat, L. Burstein, M. Schmidt, J. Lampert, C. Erk, B. Markovsky, D.T. Major, D. Aurbach, From Surface ZrO<sub>2</sub> Coating to Bulk Zr Doping by High Temperature Annealing of Nickel-Rich Lithiated Oxides and Their Enhanced Electrochemical Performance in Lithium Ion Batteries. *Adv. Energy Mater.*, **2018**, 8 (4), 1701682.

- (121) W. Liu, M. Wang, X. long Gao, W. Zhang, J. Chen, H. Zhou, X. Zhang, Improvement of the high-temperature, high-voltage cycling performance of  $\text{LiNi}_{0.5}\text{Co}_{0.2}\text{Mn}_{0.3}\text{O}_2$  cathode with  $\text{TiO}_2$  coating. *J. Alloys Compd.*, **2012**, *543*, 181-188.
- (122) R. Zhao, J. Liang, J. Huang, R. Zeng, J. Zhang, H. Chen, G. Shi, Improving the Ni-rich  $\text{LiNi}_{0.5}\text{Co}_{0.2}\text{Mn}_{0.3}\text{O}_2$  cathode properties at high operating voltage by double coating layer of  $\text{Al}_2\text{O}_3$  and  $\text{AlPO}_4$ . *J. Alloys Compd.*, **2017**, *724*, 1109-1116.
- (123) S.-H. Lee, C.S. Yoon, K. Amine, Y.-K. Sun, Improvement of long-term cycling performance of  $\text{Li}[\text{Ni}_{0.8}\text{Co}_{0.15}\text{Al}_{0.05}]\text{O}_2$  by  $\text{AlF}_3$  coating. *J. Power Sources*, **2013**, *234*, 201-207.
- (124) T. Kim, L.K. Ono, Y. Qi, Elucidating the Mechanism Involved in the Performance Improvement of Lithium-Ion Transition Metal Oxide Battery by Conducting Polymer. *Adv. Mater. Interfaces*, **2019**, *6* (7), 1801785.
- (125) F. Wu, J. Liu, L. Li, X. Zhang, R. Luo, Y. Ye, R. Chen, Surface modification of Li-rich cathode materials for lithium-ion batteries with a PEDOT: PSS conducting polymer. *ACS Appl. Mater. Interfaces*, **2016**, *8* (35), 23095-23104.
- (126) S.H. Ju, I.-S. Kang, Y.-S. Lee, W.-K. Shin, S. Kim, K. Shin, D.-W. Kim, Improvement of the cycling performance of  $\text{LiNi}_{0.6}\text{Co}_{0.2}\text{Mn}_{0.2}\text{O}_2$  cathode active materials by a dual-conductive polymer coating. *ACS Appl. Mater. Interfaces*, **2014**, *6* (4), 2546-2552.
- (127) Y.-S. Lee, W.-K. Shin, A.G. Kannan, S.M. Koo, D.-W. Kim, Improvement of the cycling performance and thermal stability of lithium-ion cells by double-layer coating of cathode materials with  $\text{Al}_2\text{O}_3$  nanoparticles and conductive polymer. *ACS Appl. Mater. Interfaces*, **2015**, *7* (25), 13944-13951.
- (128) Y. Cao, X. Qi, K. Hu, Y. Wang, Z. Gan, Y. Li, G. Hu, Z. Peng, K. Du, Conductive polymers encapsulation to enhance electrochemical

- performance of Ni-rich cathode materials for Li-ion batteries. *ACS Appl. Mater. Interfaces*, **2018**, *10* (21), 18270-18280.
- (129) S. Chen, T. He, Y. Su, Y. Lu, L. Bao, L. Chen, Q. Zhang, J. Wang, R. Chen, F. Wu, Ni-rich  $\text{LiNi}_{0.8}\text{Co}_{0.1}\text{Mn}_{0.1}\text{O}_2$  oxide coated by dual-conductive layers as high performance cathode material for lithium-ion batteries. *ACS Appl. Mater. Interfaces*, **2017**, *9* (35), 29732-29743.
- (130) X. Xiong, D. Ding, Z. Wang, B. Huang, H. Guo, X. Li, Surface modification of  $\text{LiNi}_{0.8}\text{Co}_{0.1}\text{Mn}_{0.1}\text{O}_2$  with conducting polypyrrole. *J. Solid State Electrochem.*, **2014**, *18* (9), 2619-2624.
- (131) D. Wang, X. Li, Z. Wang, H. Guo, Y. Xu, Y. Fan, Co-modification of  $\text{LiNi}_{0.5}\text{Co}_{0.2}\text{Mn}_{0.3}\text{O}_2$  cathode materials with zirconium substitution and surface polypyrrole coating: towards superior high voltage electrochemical performances for lithium ion batteries. *Electrochim. Acta*, **2016**, *196*, 101-109.
- (132) S.-L. Cai, W.-G. Zhang, R.N. Zuckermann, Z.-T. Li, X. Zhao, Y. Liu, The Organic Flatland—Recent Advances in Synthetic 2D Organic Layers. *Adv. Mat.*, **2015**, *27* (38), 5762-5770.
- (133) Z. Xiang, D. Cao, L. Dai, Well-defined two dimensional covalent organic polymers: rational design, controlled syntheses, and potential applications. *Polym. Chem.*, **2015**, *6* (11), 1896-1911.
- (134) X. Zhuang, Y. Mai, D. Wu, F. Zhang, X. Feng, Two-Dimensional Soft Nanomaterials: A Fascinating World of Materials. *Adv. Mat.*, **2015**, *27* (3), 403-427.
- (135) H. Wang, Z. Zeng, P. Xu, L. Li, G. Zeng, R. Xiao, Z. Tang, D. Huang, L. Tang, C. Lai, Recent progress in covalent organic framework thin films: fabrications, applications and perspectives. *Chem. Soc. Rev.*, **2019**, *48* (2), 488-516.
- (136) S.-Y. Ding, W. Wang, Covalent organic frameworks (COFs): from design to applications. *Chem. Soc. Rev.*, **2013**, *42* (2), 548-568.

- (137) C.S. Diercks, O.M. Yaghi, The atom, the molecule, and the covalent organic framework. *Science*, **2017**, 355 (6328), eaal1585.
- (138) M.N. Jackson, S. Oh, C.J. Kaminsky, S.B. Chu, G. Zhang, J. T. Miller, Y. Surendranath, Strong Electronic Coupling of Molecular Sites to Graphitic Electrodes via Pyrazine Conjugation. *J. Am. Chem. Soc.*, **2018**, 140 (3), 1004-1010.
- (139) J.-H. Shim, C.-Y. Kim, S.-W. Cho, A. Missiul, J.-K. Kim, Y. J. Ahn, S. Lee, Effects of heat-treatment atmosphere on electrochemical performances of Ni-rich mixed-metal oxide ( $\text{LiNi}_{0.80}\text{Co}_{0.15}\text{Mn}_{0.05}\text{O}_2$ ) as a cathode material for lithium ion battery. *Electrochim. Acta*, **2014**, 138, 15-21.
- (140) C. C. Pereira, R. Nobrega, C. P. Borges, Membrane formation with presence of Lewis acid–base complexes in polymer solution. *J. Appl. Polym. Sci.*, **2002**, 83 (9), 2022-2034.
- (141) J. Kim, H. Cho, H. Y. Jeong, H. Ma, J. Lee, J. Hwang, M. Park, J. Cho, Self-Induced Concentration Gradient in Nickel-Rich Cathodes by Sacrificial Polymeric Bead Clusters for High-Energy Lithium-Ion Batteries. *Adv. Energy Mater.*, **2017**, 7 (12), 1602559.
- (142) R. Amin, Y.-M. Chiang, Characterization of electronic and ionic transport in  $\text{Li}_{1-x}\text{Ni}_{0.33}\text{Mn}_{0.33}\text{Co}_{0.33}\text{O}_2$  (NMC333) and  $\text{Li}_{1-x}\text{Ni}_{0.50}\text{Mn}_{0.20}\text{Co}_{0.30}\text{O}_2$  (NMC523) as a function of Li content. *J. Electrochem. Soc.*, **2016**, 163 (8), A1512-A1517.
- (143) P. Jehnichen, K. Wedlich, C. Korte, Degradation of high-voltage cathodes for advanced lithium-ion batteries—differential capacity study on differently balanced cells. *Sci. Technol. Adv. Mat.*, **2019**, 20 (1), 1-9.
- (144) J.-H. Shim, Y.-M. Kim, M. Park, J. Kim, S. Lee, Reduced Graphene Oxide-Wrapped Nickel-Rich Cathode Materials for Lithium Ion Batteries. *ACS Appl. Mater. Interfaces*, **2017**, 9 (22), 18720-18729.

## Abstract in Korean

### 초 록

현대 사회에서 전기 자동차 시장의 급작스런 성장과 초소형 휴대 전자 기기들의 출현으로 인하여 높은 에너지 밀도를 가지며 원자재 가격이 저렴하고 충방전 수명이 우수한 리튬 전지의 필요성이 대두되고 있다. 높은 에너지 밀도를 가지고 있는 차세대 리튬 전지의 충방전 수명을 향상 시키기 위해서는 전해질과 양극 간 계면 제어를 통해 부반응을 막는 것이 필수적이다.

제 2장에서는 리튬-산소에서 가장 큰 이슈인 충전과전압을 감소시키기 위한 방법으로 heme 구조의 촉매를 양극에 부착하였다. Heme 구조의 리간드를 azide와 thiocyanate로 변형시킴에 따라 Fe 활성점에서의 electrostatic potential이 달라지게 된다. 이에 lewis acidity가 다른 각각의 촉매를 이용하여 과산화리튬 분해 반응이 달라지는 것을 밀도범함수이론 (Density functional Theory)로 계산하였고 lewis acidity 와 충전과전압 감소 및 수명 성능 향상의 관계를 제시하였다.

제 3장에서는 high-Ni NCM 의 충방전 사이클 중 구조적 불안정성을 해결하기 위한 방안으로 pyrazine-linked covalent organic framework (Pyr-2D) 을 high-Ni NCM 의 표면에 코팅하였다. Pyr-2D 는 이온 및 전자 전도도가 있고 매우 얇은 코팅층을 형성 할 수 있어 무기물로 이루어진 기존 코팅 방법에 비해 이점이 있다. 더욱이 Pyr-2D 를 합성하는 과정에서 NCM 표면에 형성된 preformed TM mixed layer는 Pyr-2D와 더불어 충방전 중에 전이금속 혼합이 일어나는 것을 방지해주는 역할을 하여 충방전 사이클 수명 향상 및 율속 특성 향상에 영향을 줄 수 있다는 것을 밝혔다.

본 연구는 리튬 배터리의 전해질/양극 계면 제어를 위한 촉매 개발과 표면 개질 방법의 논리적 접근 방향을 제시하고 충방전 수명 특성 향상에 미치는 영향을 분석하여 향후 전해질/양극 계면 제어 연구의 발전에 기여 할 것이라고 기대한다.

**주요어:** 양극 촉매, 양극 코팅, 전해질/양극 계면, 리튬-산소 배터리, 리튬 이온 배터리

**학 번:** 2016-39189